Deciphering the Genetic Code of Neuronal Type Connectivity: A Bilinear Modeling Approach

Mu Qiao
LinkedIn, Mountain View, CA, 94043
muqiao0626@gmail.com

Abstract

Understanding how different neuronal types connect and communicate is critical to interpreting brain function and behavior. However, it has remained a formidable challenge to decipher the genetic underpinnings that dictate the specific connections formed between neuronal types. To address this, we propose a novel bilinear modeling approach that leverages the architecture similar to that of recommendation systems. Our model transforms the gene expressions of presynaptic and postsynaptic neuronal types, obtained from single-cell transcriptomics, into a cross-correlation matrix. The objective is to construct this cross-correlation matrix that closely mirrors a connectivity matrix, derived from connectomic data, reflecting the known anatomical connections between these neuronal types. When tested on a dataset of *Caenorhabditis elegans*, our model achieved a performance comparable to, if slightly better than, the previously proposed spatial connectome model (SCM) in reconstructing electrical synaptic connectivity based on gene expressions. Through a comparative analysis, our model not only captured all genetic interactions identified by the SCM but also inferred additional ones. Applied to a mouse retinal neuronal dataset, the bilinear model successfully recapticulated recognized connectivity motifs between bipolar cells and retinal ganglion cells, and provided interpretable insights into genetic interactions shaping the connectivity. Specifically, it identified unique genetic signatures associated with different connectivity motifs, including genes important to cell-cell adhesion and synapse formation, highlighting their role in orchestrating specific synaptic connections between these neurons. Our work establishes an innovative computational strategy for decoding the genetic programming of neuronal type connectivity. It not only sets a new benchmark for single-cell transcriptomic analysis of synaptic connections but also paves the way for mechanistic studies of neural circuit assembly and genetic manipulation of circuit wiring.

1 Introduction

One of the fundamental objectives in neuroscience is understanding how diverse neuronal cell types establish connections to form functional circuits. This understanding serves as a cornerstone for decoding how the nervous system processes information and coordinates responses to stimuli [1]. Despite this, the genetic mechanisms determining the specific connections between distinct neuronal types, especially within complex brain structures, remains elusive [2, 3].

Recent advances in transcriptomics and connectomics provide opportunities to probe this. Single-cell transcriptomics enables high-resolution profiling of gene expressions across neuronal types [4, 5], while connectomic data offers detailed maps quantifying connections between neuronal cell types [6, 7, 8]. However, the challenge of linking gene expressions derived from single-cell transcriptomics

Preprint.

to neuronal type connectivity evident from connectomic data to uncover the genetic underpinnings has yet to be fully addressed.

Drawing inspiration from the field of machine learning, particularly recommendation systems, we introduce a bilinear model to bridge this gap. This model, in the context of recommendation systems, has been successful in capturing intricate user-item interactions [9]. By treating the gene expressions of pre- and post-synaptic neurons and their connectivity akin to users, items, and their ratings, we adapt the architecture of recommendation systems to the neurobiological domain. We hypothesize that a similar model could capture the complex relationships between genetic patterns of presynaptic and postsynaptic neurons and their connectivity.

This bilinear modeling approach was first applied to a *Caenorhabditis elegans* (*C. elegans*) neuronal dataset, where it not only matched but slightly outperformed the spatial connectome model (SCM) in reconstructing the connectivity of electrical synapses or gap junctions from innexin gene expressions. Notably, it revealed additional genetic interactions beyond those uncovered by the SCM. When extended to mouse retinal neurons, we demonstrate that it could effectively reconstruct synaptic connectivity between bipolar cells (BCs) and retinal ganglion cells (RGCs) from their gene expressions. The model not only unveils connectivity motifs between BCs and RGCs but also provides biologically meaningful insights into candidate genes and the genetic interactions that orchestrate this connectivity. Furthermore, our model predicts potential BC partners for RGC transcriptomic types, with these predictions aligned substantially with functional descriptions of these cell types from previous studies. Collectively, this work significantly contributes to the ongoing exploration of the genetic code underlying neuronal connectivity and suggests a potential paradigm shift in the analysis of single-cell transcriptomic data in neuroscience.

2 Background and Related Work

2.1 Synaptic Specificity

The intricate neural networks that form the basis of our nervous system are a product of specific synaptic connections between different types of neurons. This specificity is not a mere coincidence but a meticulously orchestrated process that underpins the functionality of the entire network [3, 10]. Each neuron can form thousands of connections, or synapses, with other neurons, and the specificity of these connections determines the neuron's function and, by extension, the network's function as a whole.

Synaptic specificity encompasses both chemical synapses ,which rely on neurotransmitter-mediated communication between pre- and post-synaptic neurons [3], and electrical synapses, where direct transmission of ions or small molecules occurs via gap junctions [10]. A classic example of chemical synaptic specificity is observed in the retina, where different types of BCs form specific synaptic connections with various types of RGCs [7, 11, 12]. These connections create parallel pathways that transform visual signals from photoreceptors to RGCs, which subsequently transmit the information to the brain [13, 14]. Meanwhile, specific gap junction connections, composed of connexins in vertebrates and innexins in invertebrates, has been observed between *C. elegans* neurons [15, 16, 17, 18, 19]. They function broadly in neural circuits of sensory processing and behavioral output [10, 20].

The genetic principles guiding the formation of these specific connections, particularly in complex brain structures, remains elusive. The brain's complexity, with its billions of neurons and trillions of synapses, poses significant challenges in identifying the specific genes and genetic mechanisms that guide the formation of these connections. Despite advances in genetic and neurobiological research, such as understanding the roles of certain recognition molecules and adhesion molecules in synaptic specificity, the genetic foundation of connectivity between neuronal types is still largely unknown [3, 21, 10].

Emerging tools and technologies offer unprecedented opportunities to unravel these mysteries. Among these, transcriptome and connectome are particularly promising [3, 22]. Transcriptome, the complete set of RNA transcripts produced by the genome, can provide valuable insights into the genes that are active in different types of neurons and at different stages of neuronal development. This can help identify candidate genes that may play a role in guiding neuronal connectivity. Connectome, on the other hand, provides a detailed map of the connections between neurons. By combining information

from transcriptome and connectome, it is possible to link specific genes to specific connections, thereby shedding light on the genetic basis of synaptic connectivity.

2.2 Previous Approaches

Prior research has reported several methodologies to unravel the genetic underpinnings of neuronal connectivity. For instance, Kaufman et al. showed a correlation between gene expression of *C. elegans* neurons and their connectivity [23], and Varadan et al. developed an entropy minimization approach for understanding the molecular logic of synaptic connectivity in *C. elegans* [24]. These models, however, did not fully account for spatial constraints for synaptic formation.

In response, subsequent studies proposed methodologies that integrate gene expressions with neuronal connectivity, taking into consideration physical contacts between neurons [25, 26, 27]. Specifically, the Spatial Connectome Model (SCM) in Kovács et al. correlates the gene expression of neurons with their connectivity via a rule matrix. This model aims to minimize the discrepancy between predicted connectivity based on gene expression, and observed connectivity. By restricting the analysis to neuron pairs that are in physical contact, the SCM transforms the original problem into a regression between the Kronecker product of the gene expression matrix and an edge list that captures neuronal connectivity [25].

Additionally, Taylor et al. introduced the network differential gene expression analysis (nDGE), a statistical method that expands upon traditional differential gene expression analysis by examining the co-expression of gene pairs between neuron pairs, comparing synaptic versus non-synaptic neuronal groups through t-tests. It incorporates physical contacts between neurons through the generation of "pseudoconnectomes" for null distribution estimation. Unlike multivariate methods such as the SCM, nDGE operates as a mass-univariate method, focusing on single gene pairs' contributions to synaptic formation without considering the complex interactions among multiple co-expressed genes. This makes nDGE's findings inherently conservative, ensuring strict control over type 1 errors but potentially underestimating the multifaceted nature of synaptic connectivity [27].

While the SCM and nDGE models have focused on the connectivity of individual neurons and were tested using *C. elegans* datasets, their generalization to neuronal cell types has not been explored. As we move from the invertebrate nervous systems to the neural architectures of vertebrates, such as those in mice or macaques, we need methodologies capable of unraveling the genetic basis of neuronal type connectivity [4, 28].

2.3 Collaborative Filtering

Our strategy draws inspiration from the concept of collaborative filtering using bilinear models, a technique fundamental to recommendation systems [29, 30]. These systems predict a user's preference for an item (e.g., a movie or product) based on user-item interaction data.

Bilinear models capture the interaction between users and items via low-dimensional latent features [9, 31]. Mathematically, for user i and item j, we denote their original features as $\boldsymbol{x}_i \in \mathbf{R}^{1\times p}$ and $\boldsymbol{y}_j \in \mathbf{R}^{1\times q}$, respectively. These features are then projected into a shared latent space with dimension d via transformations $\boldsymbol{x}_i\boldsymbol{A}$ (where $\boldsymbol{A} \in \mathbf{R}^{p\times d}$) and $\boldsymbol{y}_j\boldsymbol{B}$ (where $\boldsymbol{B} \in \mathbf{R}^{q\times d}$). The predicted rating of the user for the item is then formulated as:

$$r_{ij} = (\boldsymbol{x}_i\boldsymbol{A})(\boldsymbol{y}_j\boldsymbol{B})^T \tag{1}$$

In the context of collaborative filtering, the goal is to optimize the transformation matrices $\boldsymbol{A}$ and $\boldsymbol{B}$ to align the predicted rating r_{ij} with the ground-truth z_{ij}. This is expressed as the following optimization problem:

$$\min_{\boldsymbol{A},\boldsymbol{B}} \sum_{ij} (z_{ij} - (\boldsymbol{x}_i\boldsymbol{A})(\boldsymbol{y}_j\boldsymbol{B})^T)^2 \tag{2}$$

Or in the matrix form:

$$\min_{\boldsymbol{A},\boldsymbol{B}} ||\boldsymbol{Z} - (\boldsymbol{X}\boldsymbol{A})(\boldsymbol{Y}\boldsymbol{B})^T||_F^2 \tag{3}$$

Here, the objective is to minimize the Frobenius norm of the residual matrix $\boldsymbol{Z} - (\boldsymbol{XA})(\boldsymbol{YB})^T$.

In our study, we interpret neuronal connectivity through the lens of recommendation systems, viewing presynaptic neurons as "users", postsynaptic neurons as "items", and the synapses formed between them as "ratings". Our chosen bilinear model extracts latent features of pre- and post-synaptic neurons from their respective gene expressions. One key advantage of the bilinear model is its capacity to assign different weights to the gene expressions of pre- and post-synaptic neurons, enabling the model to capture not just homogeneous but also complex, heterogeneous interactions fundamental to understanding neuronal connectivity. Prior studies have highlighted such heterogeneous interactions, noting the formation of connections between pre- and post-synaptic neurons expressing different cadherins, indicative of a heterogeneous adhesion process [32, 33].

3 Bilinear Model for Neuronal Type Connectivity

We discuss the bilinear model for neuronal type connectivity in the following two scenarios: the first in which gene expression and connectivity of each cell are known simultaneously and the second where connectivity and gene expressions of neuronal types are from different sources. The bilinear models for these two situations are illustrated in Figure 1.

3.1 Gene Expression and Connectivity of Each Cell are Known Simultaneously

3.1.1 Objective Function

We begin with an ideal scenario where both the gene expression profiles and connectivity of individual cells are known concurrently. In this setting, we have a presynaptic neuronal types and b postsynaptic neuronal types, indexed by i and j, respectively. Each type contains a number of neurons, signified as n_i for presynaptic and n_j for postsynaptic types. The gene expression vector for the kth cell in the presynaptic type i is designated as $\boldsymbol{x}_{(ik)}$, where $k \in 1, 2, ..., n_i$, while for the lth cell in postsynaptic type j, it is $\boldsymbol{y}_{(jl)}$ with $l \in 1, 2, ..., n_j$. We depict the connectivity metric between a presynaptic neuron and a postsynaptic neuron as $z_{(ik)(jl)}$.

Drawing from the principles of collaborative filtering, we develop the following optimization objective:

$$\min_{\boldsymbol{A},\boldsymbol{B}} \sum_{i=1}^{a} \sum_{j=1}^{b} \left(\frac{1}{n_i n_j} \sum_{k=1}^{n_i} \sum_{l=1}^{n_j} (z_{(ik)(jl)} - (\boldsymbol{x}_{(ik)}\boldsymbol{A})(\boldsymbol{y}_{(jl)}\boldsymbol{B})^T)^2 \right) \tag{4}$$

Here, $\boldsymbol{A}$ and $\boldsymbol{B}$ denote the transformation matrices we aim to learn. This formula can also be expressed in its matrix form as:

$$\min_{\boldsymbol{A},\boldsymbol{B}} ||\boldsymbol{W} \odot (\boldsymbol{Z} - (\boldsymbol{XA})(\boldsymbol{YB})^T)||_F^2 \tag{5}$$

In this equation, $\boldsymbol{W}$ symbolizes a weight matrix where each element $w_{(ik)(jl)} = \frac{1}{\sqrt{n_i n_j}}$. As our study focuses on the genetic code of pre- and post-synaptic neuronal types rather than individual neurons, this weight matrix ensures that the model does not disproportionately favor neuronal types with a greater number of neurons over rarer types. Note that this formulation can be generalized to individual cell level analysis by treating each cell as a type and setting $n_i = n_j = 1$, thus allowing exploration of genetic underpinnings of connectivity at the single-cell resolution.

In the context of high dimensionality of gene expressions, the bilinear model may face a common issue in machine learning called multicollinearity, a condition where one or more predictor variables are highly correlated. To mitigate this, we can perform principal component analysis (PCA) on the gene expression vectors, transforming them into a new coordinate system and removing components with negligible eigenvalues to reduce redundant information. Alternatively, we can apply regularization techniques, such as L2 regularization (Ridge) or L1 regularization (Lasso) to effectively manage the multicollinearity. These regularization methods work by imposing a penalty on the size of the linear coefficients in the model, thereby shrinking the coefficients and stabilizing their estimates.

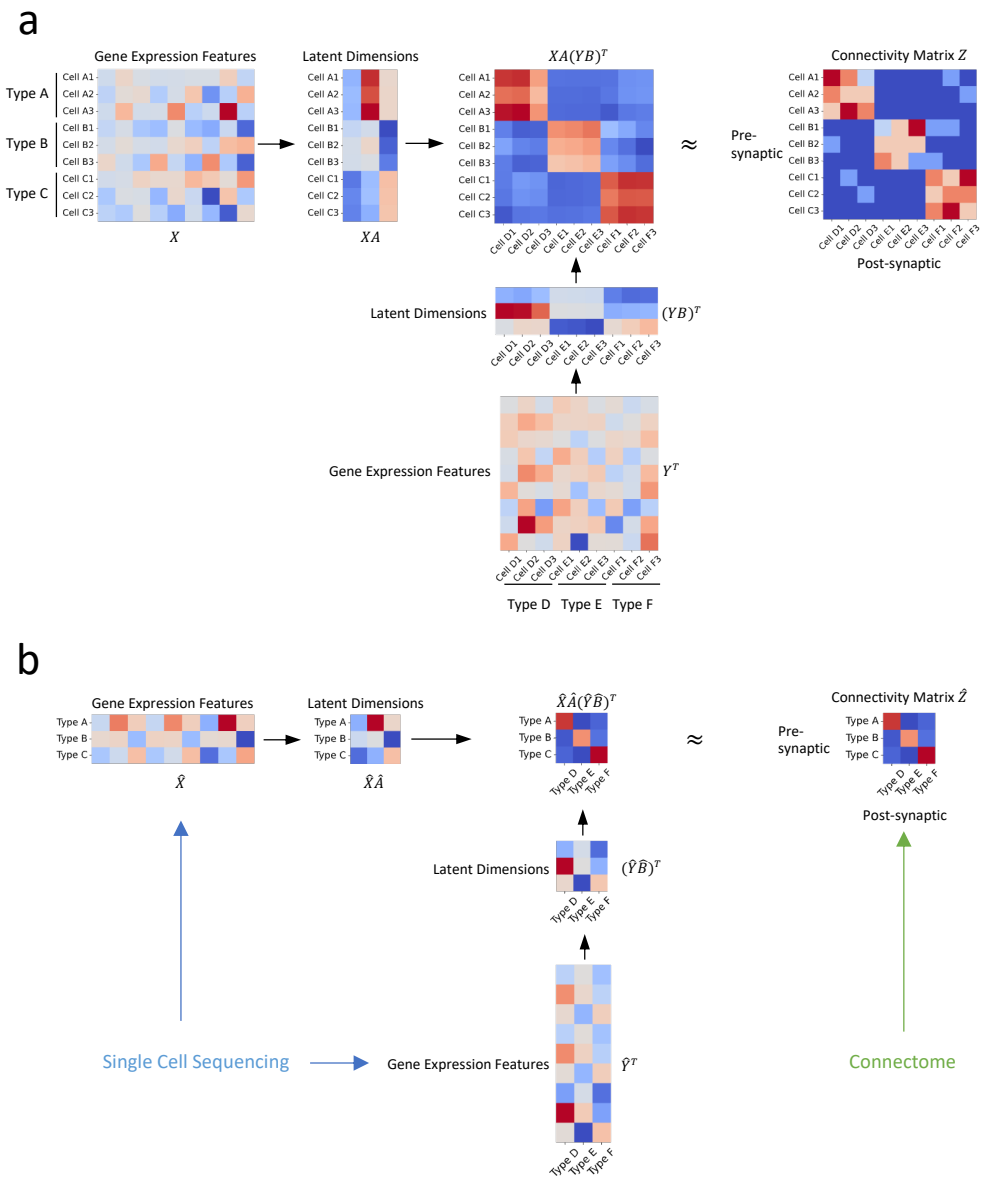

Figure 1: Illustration of our approach. (a) In an ideal scenario where gene expression profiles and connectivity data of individual cells are available simultaneously, we establish the relationship between connectivity and gene expression profiles via two transformation matrices $\boldsymbol{A}$ and $\boldsymbol{B}$ (b) In practical situations where the gene expression profiles are derived from distinct sources, such as single-cell transcriptomic and connectomic data, we propose that the connectivity of individual cells and their latent gene expression features can be approximated by the averages of their corresponding cell types, and establish their relationship through transformation matrices $\hat{\boldsymbol{A}}$ and $\hat{\boldsymbol{B}}$.

3.1.2 Optimization Algorithm

Incorporating L2 regularization, we minimize the following loss function with regularization hyper-parameters λ_A and λ_B:

$$L(\boldsymbol{A}, \boldsymbol{B}) = ||\boldsymbol{W} \odot (\boldsymbol{Z} - (\boldsymbol{X}\boldsymbol{A})(\boldsymbol{Y}\boldsymbol{B})^T)||_F^2 + \frac{\lambda_A}{2}||\boldsymbol{A}||_F^2 + \frac{\lambda_B}{2}||\boldsymbol{B}|_F^2 \tag{6}$$

To optimize this function, we propose an alternative gradient descent algorithm. This algorithm alternates between updating the transformation matrices $\boldsymbol{A}$ and $\boldsymbol{B}$, using the gradient descent optimization method.

The algorithm begins by initializing transformation matrices $\boldsymbol{A}$ and $\boldsymbol{B}$ using random values drawn from a standard normal distribution. The central aspect of the algorithm is an iterative loop that alternates the updates of $\boldsymbol{A}$ and $\boldsymbol{B}$. During each iteration, the algorithm first computes the predicted connectivity metric $\boldsymbol{Z}$ using the current estimates of $\boldsymbol{A}$ and $\boldsymbol{B}$. Subsequently, the gradient of the loss function with respect to the transformation matrices is calculated, and the matrices are updated by moving in the negative gradient's direction. This iterative process is repeated until the transformation matrices $\boldsymbol{A}$ and $\boldsymbol{B}$ converge to a steady solution. Upon completion, the algorithm yields the optimized transformation matrices.

This gradient descent-based algorithm provides a computationally efficient solution to the bilinear mapping problem between gene expression profiles and connectivity metrics. As a result, it produces associations between gene expression profiles of cell types and their connectivity.

Algorithm 1 Alternative Gradient Descent (AGD) for 4.1

procedure AGD($\boldsymbol{Z}, \boldsymbol{X}, \boldsymbol{Y}, d, r, \lambda_A, \lambda_B$) ▷ d: latent space dimension; r: learning rate
  $q \leftarrow$ second dimension of $\boldsymbol{X}$
  $p \leftarrow$ second dimension of $\boldsymbol{Y}$
  Initialize $\boldsymbol{A}$ with random values of size (q, d)
  Initialize $\boldsymbol{B}$ with random values of size (p, d)
  while not converged **do**
    $\hat{\boldsymbol{Z}} \leftarrow \boldsymbol{X}\boldsymbol{A}(\boldsymbol{Y}\boldsymbol{B})^T$ ▷ $\hat{\boldsymbol{Z}}$: prediction of $\bar{\boldsymbol{Z}}$
    Compute $\boldsymbol{A}_{\text{grad}} \leftarrow 2\boldsymbol{X}^T(\boldsymbol{W} \odot (\hat{\boldsymbol{Z}} - \boldsymbol{Z}))\boldsymbol{Y}\boldsymbol{B} + \lambda_A \boldsymbol{A}$
    Update $\boldsymbol{A} \leftarrow \boldsymbol{A} - r * \boldsymbol{A}_{\text{grad}}$
    Compute $\boldsymbol{B}_{\text{grad}} \leftarrow 2\boldsymbol{Y}^T(\boldsymbol{W} \odot (\hat{\boldsymbol{Z}} - \boldsymbol{Z}))^T\boldsymbol{X}\boldsymbol{A} + \lambda_B \boldsymbol{B}$
    Update $\boldsymbol{B} \leftarrow \boldsymbol{B} - r * \boldsymbol{B}_{\text{grad}}$
  end while
  return $\boldsymbol{A}$, $\boldsymbol{B}$
end procedure

3.2 Connectivity and Gene Expressions of Neuronal Types are from Different Sources

3.2.1 Objective Function

In real scenarios, gene expression profiles and connectivity information are often derived from separate sources, such as single-cell sequencing [34, 35] and connectome data [7, 36, 37]. Bridging these datasets requires classifying neurons into cell types based on their gene expression profiles and morphological characteristics. These cell types from different sources are subsequently aligned according to established biological knowledge (e.g., specific gene markers are known to be expressed in certain morphologically-defined cell types [38]).

The primary challenge in this scenario is that, while we can align cell types (denoted by indices i and j in equation 4), we are unable to associate individual cells (represented by indices k and l in equation 4). To tackle this issue, we adopt a simplifying assumption that the connectivity and latent gene expression features of individual cells can be approximated by the averages of their corresponding cell types. This premise hinges on the notion that the connectivity metrics and latent gene expression features of individual cells are close enough to the mean value of their corresponding cell types.

As a result, our optimization objective in equation 4 becomes:

$$\min_{\boldsymbol{A},\boldsymbol{B}} \sum_{i=1}^{a} \sum_{j=1}^{b} (z_{(i.)(j.)} - (\boldsymbol{x}_{(i.)}\boldsymbol{A})(\boldsymbol{y}_{(j.)}\boldsymbol{B})^T)^2 \tag{7}$$

In this equation, $z_{(i.)(j.)}$ denotes the mean connectivity metric between presynaptic cell type i and postsynaptic cell type j. Meanwhile, $\boldsymbol{x}_{(i.)}$ and $\boldsymbol{y}_{(j.)}$ represent the average gene expressions of cell types i and j respectively.

While optimizing the transformation matrices $\boldsymbol{A}$ and $\boldsymbol{B}$, we impose constraints on these matrices to ensure that the variance of latent gene expression features within each neuronal type is minimized. Specifically, we define ϵ as a small enough value and impose the following constraints on $\boldsymbol{A}$:

$$||\boldsymbol{A}^T \boldsymbol{\Sigma}_x \boldsymbol{A}||_F^2 \leq \epsilon \tag{8}$$

where

$$\boldsymbol{\Sigma}_x = \sum_{i=1}^{a} (\frac{1}{n_i} \sum_{k=1}^{n_i} (\boldsymbol{x}_{(ik)} - \boldsymbol{x}_{(i.)})^T (\boldsymbol{x}_{(ik)} - \boldsymbol{x}_{(i.)})) \tag{9}$$

and $\boldsymbol{B}$:

$$||\boldsymbol{B}^T \boldsymbol{\Sigma}_y \boldsymbol{B}||_F^2 \leq \epsilon \tag{10}$$

where

$$\boldsymbol{\Sigma}_y = \sum_{j=1}^{b} (\frac{1}{n_j} \sum_{l=1}^{n_j} (\boldsymbol{y}_{(jl)} - \boldsymbol{y}_{(j.)})^T (\boldsymbol{y}_{(jl)} - \boldsymbol{y}_{(j.)})) \tag{11}$$

These conditions assure that the latent gene expression features of individual cells are proximate enough to the average value within their respective cell types. With these constraints in mind, we formulate the optimization problem as follows:

$$\min_{\boldsymbol{A},\boldsymbol{B}} ||\bar{\boldsymbol{Z}} - \bar{\boldsymbol{X}}\boldsymbol{A}(\bar{\boldsymbol{Y}}\boldsymbol{B})^T||_F^2, \quad s.t. ||\boldsymbol{A}^T \boldsymbol{\Sigma}_x \boldsymbol{A}||_F^2 \leq \epsilon, ||\boldsymbol{B}^T \boldsymbol{\Sigma}_y \boldsymbol{B}||_F^2 \leq \epsilon \tag{12}$$

In this equation, $\bar{\boldsymbol{X}} \in \mathbf{R}^{a \times p}$ denotes the average gene expressions of the a presynaptic cell types, wherein each element $\bar{x}_{im}$ is indicative of the average gene expression feature m within cell type i. Likewise, $\bar{\boldsymbol{Y}} \in \mathbf{R}^{b \times q}$ represents the average gene expressions of the b postsynaptic cell types, with each element $\bar{y}_{jm}$ signifying the average gene expression feature m in cell type j.

In practical application, we approximate $\boldsymbol{\Sigma}_x$ and $\boldsymbol{\Sigma}_y$ with their diagonal estimates $diag(\hat{\sigma}_{x_1}^2, \hat{\sigma}_{x_2}^2, ..., \hat{\sigma}_{x_p}^2)$ and $diag(\hat{\sigma}_{y_1}^2, \hat{\sigma}_{y_2}^2, ..., \hat{\sigma}_{y_q}^2)$ [39, 40]. We then transform the initial optimization problem into the following:

$$\min_{\hat{\boldsymbol{A}},\hat{\boldsymbol{B}}} ||\bar{\boldsymbol{Z}} - \hat{\boldsymbol{X}}\hat{\boldsymbol{A}}(\hat{\boldsymbol{Y}}\hat{\boldsymbol{B}})^T||_F^2, \quad s.t. ||\hat{\boldsymbol{A}}^T \hat{\boldsymbol{A}}||_F^2 \leq \epsilon, ||\hat{\boldsymbol{B}}^T \hat{\boldsymbol{B}}||_F^2 \leq \epsilon \tag{13}$$

Here, elements in $\hat{\boldsymbol{X}} \in \mathbf{R}^{a \times p}$ are defined as $\hat{x}_{im} = \frac{\bar{x}_{im}}{\hat{\sigma}_{x_m}}$ and elements in $\hat{\boldsymbol{Y}} \in \mathbf{R}^{b \times q}$ are given by $\hat{y}_{im} = \frac{\bar{y}_{im}}{\hat{\sigma}_{y_m}}$. The optimization of this formulation tends to be computationally more tractable.

In summary, our methodology adapts when gene expression profiles and the connectivity matrix originate from distinct sources. Instead of aligning at the level of individual cells, we focus on the alignment of neuronal types. We achieve this by mapping gene expressions into a latent space via transformation matrices $\hat{\boldsymbol{A}}$ and $\hat{\boldsymbol{B}}$, with the optimization process aiming to minimize the discrepancies between these two sources of information while maintaining consistency of the gene expression features within individual neuronal types.

3.2.2 Optimization Algorithm

To solve the optimization problem as outlined in equation 13, we construct the following loss function:

$$L(\hat{\boldsymbol{A}}, \hat{\boldsymbol{B}}) = ||\bar{\boldsymbol{Z}} - \hat{\boldsymbol{X}}\hat{\boldsymbol{A}}(\hat{\boldsymbol{Y}}\hat{\boldsymbol{B}})^T||_F^2 + \frac{\lambda_A}{2}||\hat{\boldsymbol{A}}^T\hat{\boldsymbol{A}}||_F^2 + \frac{\lambda_B}{2}||\hat{\boldsymbol{B}}^T\hat{\boldsymbol{B}}||_F^2 \tag{14}$$

where λ_A and λ_B are hyperparameters whose optimal values are determined through a grid search.

To optimize this loss function, we employ an alternative gradient descent algorithm analogous to that described in section 3.1.2, by iteratively updating the transformation matrices $\hat{\boldsymbol{A}}$ and $\hat{\boldsymbol{B}}$.

Algorithm 2 Alternative Gradient Descent (AGD) for 4.2

procedure AGD($\bar{\boldsymbol{Z}}, \hat{\boldsymbol{X}}, \hat{\boldsymbol{Y}}, d, r, \lambda_A, \lambda_B$) ▷ d: latent space dimension; r: learning rate
  $q \leftarrow$ second dimension of $\hat{\boldsymbol{X}}$
  $p \leftarrow$ second dimension of $\hat{\boldsymbol{Y}}$
  Initialize $\hat{\boldsymbol{A}}$ with random values of size (q, d)
  Initialize $\hat{\boldsymbol{B}}$ with random values of size (p, d)
  while not converge **do**
    $\hat{\boldsymbol{Z}} \leftarrow \hat{\boldsymbol{X}}\hat{\boldsymbol{A}}(\hat{\boldsymbol{Y}}\hat{\boldsymbol{B}})^T$ ▷ $\hat{\boldsymbol{Z}}$: prediction of $\bar{\boldsymbol{Z}}$
    Compute $\hat{\boldsymbol{A}}_{grad} \leftarrow \hat{\boldsymbol{X}}^T(\hat{\boldsymbol{Z}} - \bar{\boldsymbol{Z}})\hat{\boldsymbol{Y}}\hat{\boldsymbol{B}} + \lambda_A\hat{\boldsymbol{A}}(\hat{\boldsymbol{A}}^T\hat{\boldsymbol{A}})$
    Update $\hat{\boldsymbol{A}} \leftarrow \hat{\boldsymbol{A}} - r * \hat{\boldsymbol{A}}_{grad}$
    Compute $\hat{\boldsymbol{B}}_{grad} \leftarrow \hat{\boldsymbol{Y}}^T(\hat{\boldsymbol{Z}} - \bar{\boldsymbol{Z}})\hat{\boldsymbol{X}}\hat{\boldsymbol{A}} + \lambda_B\hat{\boldsymbol{B}}(\hat{\boldsymbol{B}}^T\hat{\boldsymbol{B}})$
    Update $\hat{\boldsymbol{B}} \leftarrow \hat{\boldsymbol{B}} - r * \hat{\boldsymbol{B}}_{grad}$
  end while
  return $\hat{\boldsymbol{A}}$, $\hat{\boldsymbol{B}}$
end procedure

4 Datasets and Pre-processing

To validate and assess the efficacy of our bilinear model, we utilized two distinct datasets available from previous studies:

4.1 Gap Junction Connectivity and Innexin Expression Data of *C. elegans* Neurons

We first used a dataset of gap junction connectivity and innexin expressions of individual *C. elegans* neurons. Derived from the work of Cook et al. [41] and subsequently analyzed by Kovács et al. [25], this dataset included expression profiles of 18 innexin genes across 184 neurons, alongside detailed gap junction connectivity between these neurons. We followed the same procedure outlined by Kovács et al. to obtain the innexin expression matrix $\boldsymbol{X}$ and $\boldsymbol{Y}$ (in this case $\boldsymbol{X} = \boldsymbol{Y}$ with the dimensions of 184×18), and the connectivity matrix between individual *C. elegans* neurons $\boldsymbol{Z}$.

To incorporate spatial constraints by considering only neuron pairs in physical contact, we extracted a contact matrix from the dataset. This was transcribed into the weight matrix $\boldsymbol{W}$ in our model, with values set to 0 for neuron pairs without physical contact and 1 for those with contact. This enabled our bilinear model to focus on the 5,592 neuron pairs that exhibit physical contacts, restricting the analysis to biologically plausible connections.

The utilization of this dataset serves a dual purpose. It not only provides a validation for our bilinear model but also enables a direct comparison with the model employed by Kovács et al., offering a comprehensive evaluation of the bilinear model in the context of established connectomic research.

4.2 Single-cell Transcriptomic and Connectomic Data of Mouse Retinal Neurons

The second dataset encompassed data of mouse retinal neurons, integrating single-cell transcriptomic data from various studies with connectomic data obtained from the EyeWire project. The data provide us with connectivity information and gene expression profiles of mouse BCs and RGCs, and are

important for applying our proposed bilinear model and testing its effectiveness in a more complex neuronal environment compared to the *C. elegans* dataset.

4.2.1 Single-cell Transcriptomic Data

The single-cell transcriptomic data include the gene expression profiles for two classes of mouse retinal neurons - presynaptic BCs as reported by Shekhar et al. [34], and postsynaptic RGCs as reported by Tran et al. [35].

Preprocessing of this data adhered to previously documented procedures [34, 35, 42]. The transcript counts within each cell were first normalized to align with the median number of the transcripts per cell, followed by a log-transformation of the normalized counts. High variable genes (HVGs) were then selected using an approach based on establishing a relationship between mean expression level and the coefficient of variance [43, 44, 45]. We focused on those cells whose types correspond with the neuronal types outlined in the connectomic data, as delineated later in Table S1, Table S2, and Table S3. This yielded two matrices, $\boldsymbol{X}$ and $\boldsymbol{Y}$, representing presynaptic BCs and postsynaptic RGCs, where each row pertains to a cell and each column represents an HVG. The dimensions of $\boldsymbol{X}$ and $\boldsymbol{Y}$ are 22453 $\times$ 17144 and 3779 $\times$ 12926, respectively.

Next, we performed a principal component analysis (PCA) on these matrices to transform the gene expression data into the principal component (PC) space. We retained only the PCs that account for a cumulative 95% of explained variance. Consequently, the gene expression of the BCs in $\boldsymbol{X}$ and the RGCs in $\boldsymbol{Y}$ were featurized by their respective PCs, resulting in matrices of dimensions 22453 $\times$ 11323 and 3779 $\times$ 3142, respectively.

Based on each cell's neuronal type, we computed the variance of gene expression features within these types. Mathematically, the variance of gene expression feature m within the BC types and the RGC types are expressed as:

$$\hat{\sigma}_{x_{im}} = \sum_{i=1}^{a}(\frac{1}{n_i}\sum_{k=1}^{n_i}(x_{(ik)m} - x_{(i.)m})^2) \tag{15}$$

$$\hat{\sigma}_{y_{jm}} = \sum_{j=1}^{b}(\frac{1}{n_j}\sum_{l=1}^{n_j}(y_{(jl)m} - y_{(j.)m})^2) \tag{16}$$

Taking $\bar{x}_{im}$ and $\bar{y}_{jm}$ to represent the average gene expression feature m of the BC type i and the RGC type j, we were able construct matrices, $\hat{\boldsymbol{X}}$ and $\hat{\boldsymbol{Y}}$, in which $\hat{x}_{im} = \frac{\bar{x}_{im}}{\hat{\sigma}_{x_m}}$ and $\hat{y}_{im} = \frac{\bar{y}_{im}}{\hat{\sigma}_{y_m}}$. In these matrics, each row represents a cell type, with the dimensions of $\hat{\boldsymbol{X}}$ being 25 $\times$ 11323 and $\hat{\boldsymbol{Y}}$ being 12 $\times$ 3142. These matrices serve to bridge the gene expression of BC types and RGC types with the connectivity matrix of these neuronal types derived from the connectomic data.

4.2.2 Connectivity Data

The connectivity matrix of neuronal types is derived from connectomic data acquired through the process of serial electron microscopy (EM)-based reconstruction of brain tissues [6, 7, 8]. From these reconstructed tissues, connectivity measurements are usually expressed as either the contact area or the number of synapses between neurons [7, 46]. When normalized to the total contact area or total number of synapses of each neuron, the resulting metric, ranging from 0 to 1, signifies the percentage of contact area or synapses formed between neurons. This normalized metric provides a quantitative connectivity measure, where 0 indicates no connectivity and 1 implies complete connectivity between two neurons.

Our analysis utilized the neural reconstruction data of mouse retinal neurons, courtesy of the EyeWire project, a crowd-sourced initiative that generates 3D reconstructions of neurons from serial section EM images [47]. This extensive dataset facilitated the derivation of a comprehensive connectivity matrix between two classes of mouse retinal neurons - BCs [37] and RGCs [36]. The data were sourced from the EyeWire Museum (https://museum.eyewire.org/), which offers detailed information for each cell in a JSON file, including attributes like "cell id", "cell type", "cell class", and "stratification". The

stratification profile describes the linear density of voxel volume as a function of the inner plexiform layer (IPL) depth [47, 37, 36].

We approximated the connectivity metric between a BC and a RGC using the cosine similarity of their stratification profiles. Let $\boldsymbol{v}_{ik}$ and $\boldsymbol{v}_{jl}$ denote the stratification profiles of the kth cell in BC type i and the lth cell in RGC type j, respectively. The connectivity metric $z_{(ik)(jl)}$ between these two neurons can be expressed as:

$$z_{(ik)(jl)} = \frac{\boldsymbol{u}_{ik}\boldsymbol{v}_{jl}}{|\boldsymbol{v}_{ik}||\boldsymbol{v}_{jl}|} \tag{17}$$

This equation represents the degree of overlap in their voxel volume profile within the IPL, resulting in the connectivity matrix $\boldsymbol{Z}$ between mouse BCs and RGCs. To allow for both positive and negative values within the matrix, we standardized $\bar{\boldsymbol{Z}}$ by subtracting the mean of $\bar{\boldsymbol{Z}}$ and then dividing by its standard deviation. Subsequently, the connectivity matrix $\bar{\boldsymbol{Z}}$ between mouse BC and RGC neuronal types was calculated, with each element $\bar{z}_{ij} = z(i.)(j.)$ representing the average of the connectivity metrics between cells of BC type i and cells of RGC type j.

4.2.3 Correspondence of Mouse Retinal Cell Types

Aligning neuronal types as annotated in the single-cell transcriptomic data and those identified in the connectomic data was informed by findings from previous studies. Notably, a one-to-one correspondence exists between BC cell types classified by Shekhar et al. [34] and Greene et al. [37]. This correspondence is presented in Table S1.

Regarding RGC types, alignment between cell types annotated in Tran et al. [35] and Bae et al. [36] was established primarily based on the findings from Goetz et al. [38]. This study presents a unified classification of mouse RGC types, based on their functional, morphological, and gene expression features. The corresponding RGC types were mainly obtained from Supplementary Table S3 of Goetz et al. (Table S2), with additions derived from Supplementary Table S1 of Tran et al., based on the expressions of genetic markers of these RGC types (Table S3).

5 Model Training, Validation, and Comparison

Our approach of training and validating the bilinear model involved an iterative optimization of transformation matrices using the AGD algorithm, as outlined in Section 3. The primary goal was to minimize the defined loss function. With the matrices initially generated from a standard normal distribution, the optimization process continued until the loss change was less than a threshold of 10^{-6}, or a maximum of 10^6 iterations were completed.

During optimization, we focused on two key hyperparameters: the regularization parameters, λ_A and λ_B, and the latent feature space dimensionality. Preliminary tests indicated that a lower loss was achieved when both regularization parameters were set equally, leading us to consolidate them into a single parameter, λ.

5.1 *C. elegans* Neuronal Dataset

For the *C. elegans* dataset, which provides simultaneous gene expression and connectivity data for individual cells, we employed the model configuration described in section 3.1. The model's hyperparameters, λ and the latent feature space dimensionality, were fine-tuned through 5-fold cross-validation, exploring a range of values for λ and different dimensions for the latent feature space. The optimal hyperparameters were identified based on the lowest validation loss observed during cross-validation (Figure S1).

Given the prior utilization of this dataset in validating the SCM proposed by Kovács et al. [25], our bilinear model was positioned for a direct comparison with the SCM. The SCM introduced a rule matrix $\boldsymbol{O}$ with the aim to minimize the discrepancy between the observed connectivity and the gene expression-based predicted connectivity $\boldsymbol{X}\boldsymbol{O}\boldsymbol{X}^T$, employing L2 regularization on $\boldsymbol{O}$. Our bilinear model echoes this approach, where we seek to minimize the divergence between the connectivity matrix and the bilinearly predicted connectivity $\boldsymbol{X}\boldsymbol{A}(\boldsymbol{X}\boldsymbol{B})^T$, with L2 regularization

imposed on matrices $\boldsymbol{A}$ and $\boldsymbol{B}$. In essence, the bilinear form decomposes the rule matrix into two lower-dimensional matrices, which represent projections onto latent dimensions.

To quantitatively compare the bilinear model's transformation matrix product $\hat{\boldsymbol{O}} = \boldsymbol{A}\boldsymbol{B}^T$ with the SCM's rule matrix $\boldsymbol{O}$, and to systematically identify the genetic interaction each model uniquely captured, we introduced the discrepancy score (DS). For each pair of corresponding entries in the matrices at indices i and j, the DS is calculated as follows:

$$DS_{ij} = \frac{|\hat{o}_{ij} - o_{ij}|}{|\hat{o}_{ij}| + |o_{ij}|} \tag{18}$$

This metric, ranging from 0 to 1, quantifies the relative discrepancy between the two matrices, normalizing it in relation to their magnitudes. A score close to 1 indicates a large discrepancy, while a score near 0 suggests a negligible difference between the entries. Through this lens, we can further scrutinize the corresponding entries with the score above a certain threshold to reveal specific genetic interactions captured by one model but potentially missed by the other.

5.2 Mouse Retinal Neuronal Dataset

The model's application to the mouse retina dataset, which involves gene expression and connectivity data from disparate sources, was facilitated by the approach outlined in section 3.2. Optimal hyperparameters were determined through 5-fold cross-validation, adjusting λ and exploring various dimensionalities for the latent feature space (Figure S2). Notably, the lowest validation loss was achieved with the dimensionality of two. Given the chosen hyperparameters, we performed the final round of training on the entire dataset to yield the definitive transformation matrices $\hat{\boldsymbol{A}}$ and $\hat{\boldsymbol{B}}$.

To assess the consistency of our model under PCA pre-processing across different replicates, we repeated the optimization procedure five times, each time adhering to the previously identified optimal hyperparameters. In the context of our solution, where $\hat{\boldsymbol{A}} = [\boldsymbol{u}_1 \quad \boldsymbol{u}_2]$ and $\hat{\boldsymbol{B}} = [\boldsymbol{v}_1 \quad \boldsymbol{v}_2]$, with vectors $\boldsymbol{u}_1, \boldsymbol{v}_1$ representing coefficients for the first latent dimension and $\boldsymbol{u}_2, \boldsymbol{v}_2$ for the second, we noted that negating the coefficients of any latent dimension in both matrices (for instance, $\hat{\boldsymbol{A}} = [-\boldsymbol{u}_1 \quad \boldsymbol{u}_2]$ and $\hat{\boldsymbol{B}} = [-\boldsymbol{v}_1 \quad \boldsymbol{v}_2]$) results in an equivalent solution. Therefore, to compare solutions across different repetitions, we calculated the absolute value of cosine similarity for each latent dimension's coefficient vectors, and reported the similarity between solutions as the average of the values across the two latent dimensions. Moreover, we recognized that swapping the positions of the coefficient vectors (yielding $\hat{\boldsymbol{A}} = [\boldsymbol{u}_2 \quad \boldsymbol{u}_1]$ and $\hat{\boldsymbol{B}} = [\boldsymbol{v}_2 \quad \boldsymbol{v}_1]$) also leads to an equivalent solution. To accommodate this, we evaluated both the original and swapped vector pairings for each repetition. The final measure of consistency was determined by taking the maximum of the two average absolute cosine similarities, ensuring a comprehensive and robust assessment of solution consistency across multiple runs.

We observed a high degree of consistency across multiple repetitions of the solutions under PCA pre-processing (Figure S3). The majority of the average absolute cosine similarity scores are close to 1, and even the minimum observed similarities are well above 0.75, suggesting that the optimization yields stable solutions.

6 Results

6.1 Comparative Analysis using *C. elegans* Neuronal Data

6.1.1 Reconstruction of *C. elegans* Gap Junction Connectivity from Innexin Expressions

Utilizing the *C. elegans* neuronal dataset, we first tried to reconstruct the gap junction connectivity network based solely on the expression profiles of innexin genes. Using $\boldsymbol{A}$ and $\boldsymbol{B}$ generated by the bilinear model, we processed the innexin expression data to predict gap junction connectivity between neuron pairs as $\boldsymbol{X}\boldsymbol{A}(\boldsymbol{Y}\boldsymbol{B})^T$ (Figure 2a). This approach was then compared to the SCM proposed by Kovács et al. [25], which used a rule matrix $\boldsymbol{O}$ to correlate gene expression with observed connectivity in the form of $\boldsymbol{X}\boldsymbol{O}\boldsymbol{X}^T$ (Figure 2b).

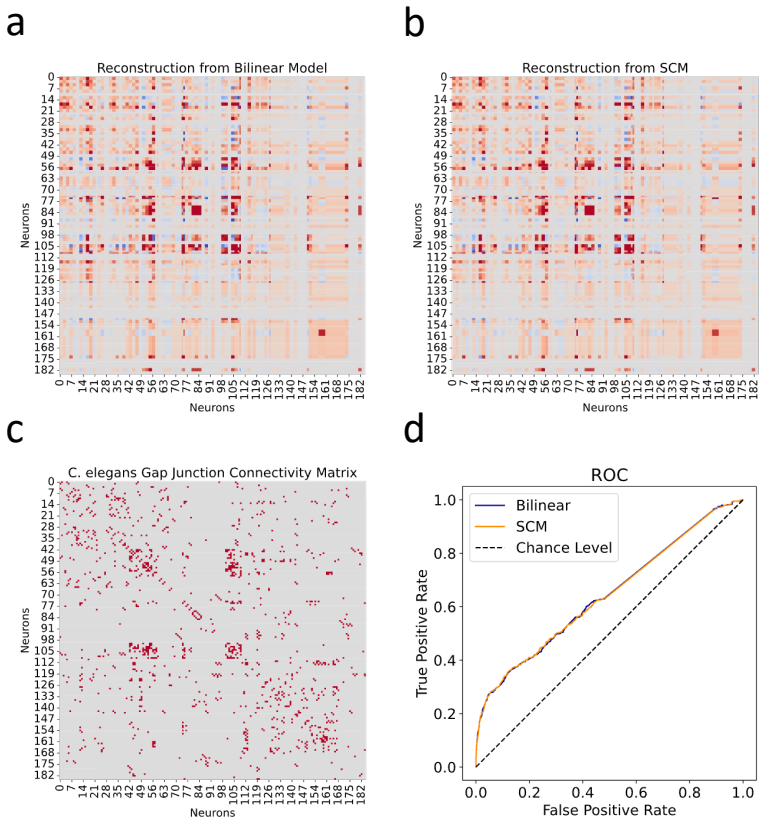

Figure 2: Reconstructed gap junction connectivity from innexin expression data. (a) Connectivity matrix predicted by the bilinear model. (b) Connectivity matrix modeled from Kovács et al.'s SCM. (c) Observed gap junction connectivity matrix, serving as ground truth. The color spectrum from red to gray denotes the spectrum from strong connections to weak or no connections. (d) ROC Curves from both the bilinear model and the SCM. Dashed line indicates the chance level.

The effectiveness of both models was evaluated against the observed gap junction connectivity matrix of *C. elegans* neurons (Figure 2c). Given the binary nature of the ground truth matrix (where 1 denotes a connection and 0 indicates its absence) and the continuous nature of reconstructed connectivity matrices from both models, we conducted Receiver Operating Characteristic (ROC) analysis. This involves varying a threshold to binarize the continuous predictions, under which the true positive rate is plotted against the false positive rate for each possible cutoff. This process yields the ROC curve, which is a graphical representation of the trade-off between sensitivity and specificity at various thresholds (Figure 2d).

Subsequently, we calculated the Area Under the ROC Curve (AUC), providing a singular value summarizing the overall predictive performance of the model across all thresholds. The ROC-AUC metric is particularly informative as it aggregates the model's effectiveness over all possible thresholds, with a score of 1 indicating perfect prediction and 0.5 denoting a performance no better than random chance. From the calculation, the bilinear model achieved a ROC-AUC score of 0.6435, slightly surpassing the SCM's score of 0.6428. While both scores are reasonably close, the slight edge of the bilinear model indicates its nuanced efficiency in mapping gene expressions to connectivity. However, it is noteworthy that both scores, while above 0.5, are substantially distant from the ideal score of 1. This observation suggests that relying exclusively on innexin expression data might be insufficient for fully capturing the detailed gap junction connectivity in *C. elegans*.

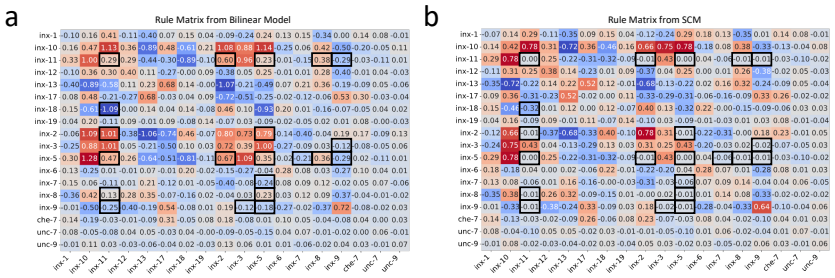

Figure 3: Genetic rules from the bilinear model and the SCM. (a) The rule matrix $\boldsymbol{A}\boldsymbol{B}^T$ derived from the bilinear model. (b) The rule matrix $\boldsymbol{O}$ from the SCM. Black boxes highlight entries with substantial differences.

6.1.2 Comparison of Rule Matrix from SCM and Bilinear Transformation Matrices

In light of the challenge in fully capturing the *C. elegans* gap junction connectivity based on innexin expression data alone, instead of analyzing connectivity motifs between *C. elegans* neurons, our focus pivoted towards exploring and comparing the genetic rules inferred by both the bilinear model and the SCM, which was also the key discussion presented in Kovács et al. [25]. As mentioned in Section 5.1 and discussed in Section 7, the product of the bilinear transformation matrices, $\hat{\boldsymbol{O}} = \boldsymbol{A}\boldsymbol{B}^T$, can be interpreted as a lower-dimensional reconstruction of the rule matrix $\boldsymbol{O}$ used in the SCM. This perspective steered us to a meticulous comparative analysis between the two matrices.

The rule matrix solved from the SCM establishes a baseline for the comparison (Figure 3b). Against that, we compared the product of the bilinear transformation matrices (Figure 3a). Visualization of the two matrices suggests a high degree of similarity between them, which is quantitatively supported by a Pearson correlation coefficient of 0.90 ($p < 0.001$), underscoring a strong alignment.

To discern specific genetic interactions uniquely characterized by each model, we applied the DS metric to corresponding matrix entries (Figure S4a). This metric, ranging from 0 (no discrepancy) to 1 (maximum discrepancy), was thresholded at 0.5 to highlight entries with substantial differences. Further, to account for the regularization effect that pushes less important coefficients toward zero, we filtered out entry pairs where both values were less than 0.1 (Figure S4b,c). The remaining pairs are highlighted in black boxes in both matrices (Figure 3).

Comparing the values of highlighted entry pairs, we found that the bilinear model not only captured all genetic interactions identified by the SCM but also inferred additional ones: certain innexins (inx-11, inx-8, inx-5, and inx-2) were implicated in co-expression patterns within connected neurons, while another set (inx-11, inx-9, inx-3, inx-5, inx-7) was associated with an avoidance pattern, suggesting a lack of co-expression in neuron pairs forming gap junctions. These findings provide extra candidates to be tested in future experiments.

6.2 Application of Bilinear Model to Mouse Retinal Neuronal Data

6.2.1 Bilinear Model Reconstructs Neuronal Type-Specific Connectivity Map from Gene Expression Profiles

In our application of the bilinear model to the mouse retinal neuronal data, upon completion of the final training process, our optimized bilinear model produced transformation matrices, $\hat{\boldsymbol{A}}$ and $\hat{\boldsymbol{B}}$. We used these matrices to project the normalized single-cell transcriptomic data, $\hat{\boldsymbol{X}}$ and $\hat{\boldsymbol{Y}}$, into a shared latent feature space. Consequently, we obtained projected representations for BC and RGC types, $\hat{\boldsymbol{X}}\hat{\boldsymbol{A}}$ and $\hat{\boldsymbol{Y}}\hat{\boldsymbol{B}}$, respectively. With these latent representations, we were able to reconstruct the cell-type-specific connectivity matrix: $\hat{\boldsymbol{X}}\hat{\boldsymbol{A}}(\hat{\boldsymbol{Y}}\hat{\boldsymbol{B}})^T$ (Figure 4a).

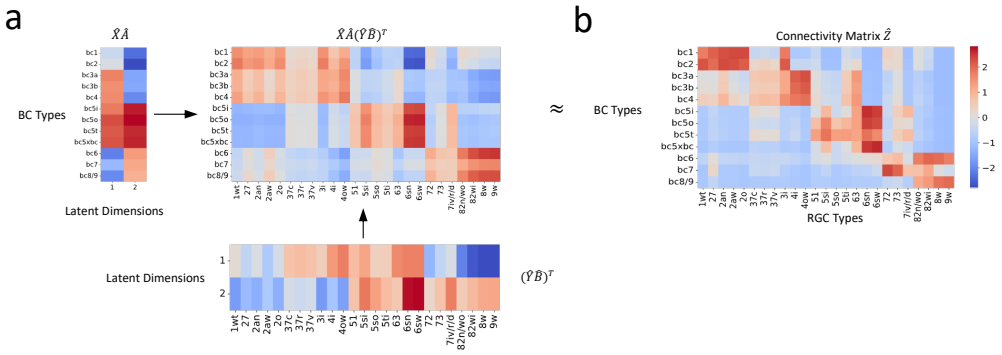

Figure 4: Reconstruction of connectivity map from gene expression profiles. (a) The reconstructed connectivity matrix, derived from the shared latent feature space projections. (b) The connectivity matrix obtained from connectomic data. Differences in color intensity represent the strength of connections, with dark red indicating strong connections and dark blue indicating weak or no connections.

To evaluate our model, we compared the reconstructed connectivity matrix with the one derived from connectomic data (Figure 4b). We calculated the Pearson correlation coefficient between entries of the two matrices to assess their agreement. The resulting correlation of 0.83 ($p < 0.001$) demonstrated a robust association between the transformed gene expression features and the connectomic data. This result attests to our model's capability in capturing the relationship between these two distinct types of biological information.

To gain insights into our model's reconstruction accuracy, we employed the DS metric to identify entries with substantial deviations between the reconstructed and the actual connectivity matrices (Figure S5a). This examination specifically quantified the extent of connections in the target matrix (positive entries) that were not captured in the model's reconstruction (negative entries) (Figure S5b,c). Notably, the analysis revealed that only a small fraction, specifically 9 out of 115 connections, were not represented in the reconstructed matrix.

6.2.2 Bilinear Model Recapitulates Recognized Connectivity Motifs

Our cross-validation procedure indicated that the optimal number of latent dimensions was two (Figure S2). This finding suggested that these two dimensions capture the essential connectivity motifs between BC and RGC types. This led us to further investigate what are these motifs and how they are different from each other.

We first reconstructed connectivity using only the first latent dimension. The first dimension appeared to emphasize connectivity patterns between BCs and RGCs that laminate within the IPL's central region, as well as those that laminate within the marginal region (Figure 5a,d,g). We then reconstructed connectivity using only the second latent dimension. Notably, the spotlight shifted to connections between BCs and RGCs that laminate within the outer and inner regions of the IPL, respectively (Figure 5b,e,i).

To confirm these observations, we further visualized BC and RGC types within the two-dimensional latent feature space (Figure 5c,f). Grouping BC and RGC types based on whether they fell within the positive or negative halves of the latent dimensions, we color-coded their stratification profiles within the IPL by group. BCs and RGCs that fell within the positive half of latent dimension 1 tend to stratify within the IPL's central region, delineated by the boundaries formed by the ON and OFF starburst amacrine cells (SACs) (Figure 5d,g). Conversely, those falling within the negative half of this dimension tend to stratify in the marginal region of the IPL. As for the second latent dimension, BCs and RGCs that fell within the positive half predominantly stratify in the inner region of the IPL (Figure 5e,i), while those within the negative half primarily stratify in the IPL's outer region.

Interestingly, these distinct connectivity motifs align with two widely recognized properties of retinal neurons: kinetic attributes that reflect the temporal dynamics (transient versus sustained responses) of

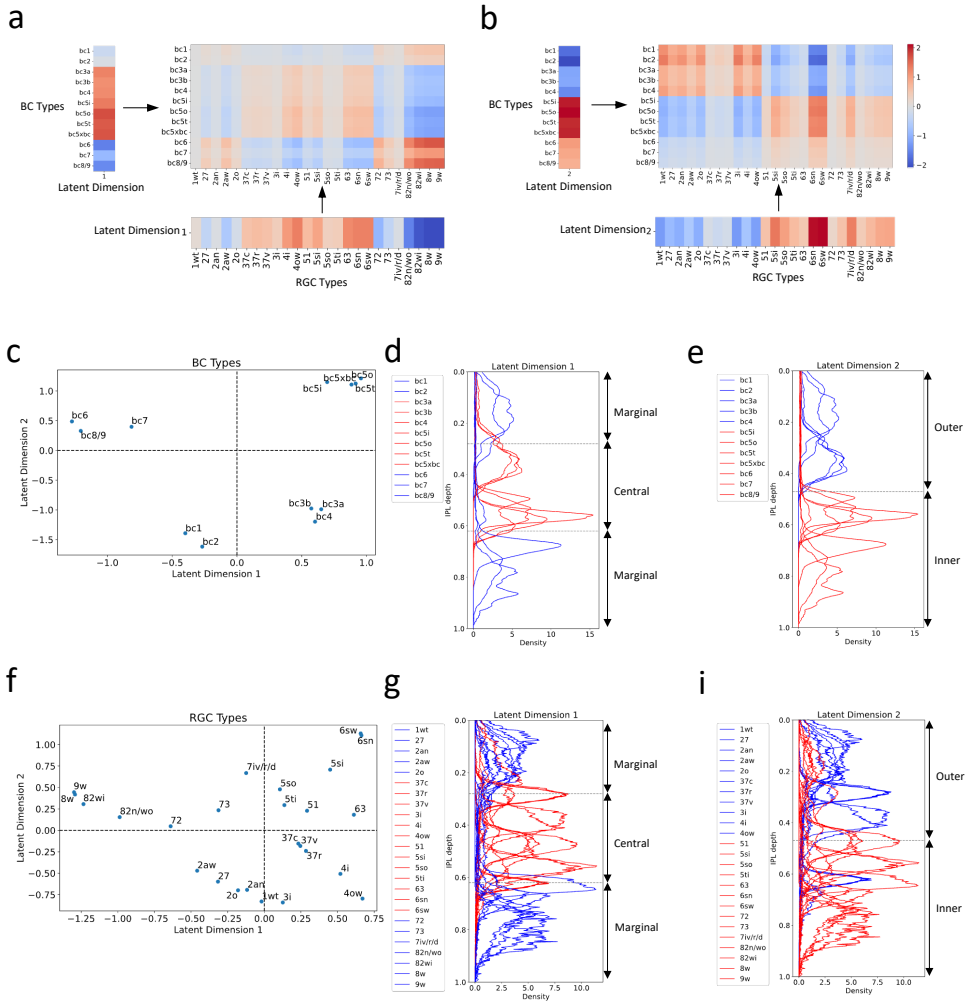

Figure 5: Distinct connectivity motifs revealed by the two latent dimensions. (a, b) The reconstructed connectivity using only latent dimension 1 or 2, respectively. Differences in color intensity represent the strength of connections. (c) BC types plotted in the latent feature space, with each point representing a specific BC type. Dashed lines indicate zero values for latent dimensions 1 and 2. (d, e) Stratification profiles of BC types in IPL, color-coded based on their positions along the first (d) or second (e) latent dimension. Red indicates BC types on the positive half, while blue indicates BC types on the negative half. (f) RGC types plotted in the latent feature space, with each point representing a specific RGC type. (g, h) Stratification profiles of RGC types in IPL, color-coded based on their positions along the first (g) or second (h) latent dimension. Dashed lines in (d) and (g) mark the positions of ON and OFF SACs [36]. BCs and RGCs stratifying between them tend to exhibit more transient responses, and those stratifying outside them exhibit more sustained responses. Dashed lines in (e) and (h) denote the boundary of the outer and inner IPL [36]. Synapses between BCs and RGCs in the outer retina mediate OFF responses, while those in the inner retina mediate ON responses.

a neuron responding to visual stimuli, and polarity (ON versus OFF responses) reflecting whether a neuron responds to the initiation or cessation of a stimulus [48, 11, 12, 49]. This correlation implies that our bilinear model has successfully captured key aspects of retinal circuitry from gene expression data.

6.2.3 Bilinear Model Reveals Interpretable Insights into Gene Signatures Associated with Different Connectivity Motifs

The inherent linearity of our bilinear model affords a significant advantage: it enables the direct interpretation of gene expressions by examining their associated weights in the model. These weights signify the importance of each gene in determining the connectivity motifs between the BC and RGC types. We identified the top 50 genes with the largest positive or negative weights for BCs and RGCs across both latent dimensions. We plotted their weights alongside their expression profiles in the respective cell types (Figure 6).

Our analysis unveiled distinct gene signatures associated with the connectivity motifs revealed by the two latent dimensions. In the first latent dimension, genes like CDH11 and EPHA3, involved in cell adhesion and axon guidance, carried high weights for BCs forming synapses in the IPL's central region. In contrast, for BCs synapsing in the marginal region, we observed high weights in the cell adhesion molecule PCDH9 and the axon guidance cue UNC5D (Figure 6a). This pattern was echoed in RGCs but involved a slightly different set of molecules. For example, in RGCs forming synapses in the IPL's central region, the cell adhesion molecule PCDH7 carried high weights, whereas for RGCs synapsing in the marginal region, cell adhesion molecules PCDH11X and CDH12 were associated with high weights (Figure 6b).

The second latent dimension revealed a comparable pattern, albeit with different gene signatures. For BCs laminating in the IPL's outer region, high weights were assigned with guidance cues such as SLIT2, NLGN1, EPHA3 and PLXNA4, as well as the adhesion molecule DSCAM. For BCs in the inner region, the adhesion molecule CNTN5 was associated with a high weight (Figure 6c). In RGCs, we noticed that guidance molecules such as PLXNA2, SLITRK6 and PLXNA4 along with adhesion modules CDH8 and LRRC4C were associated with high weights for cells forming synapses in the IPL's outer region. In contrast, the adhesion molecule SDK2 was among the top genes for RGCs laminating and forming synapses in the IPL's inner region (Figure 6d). Some of these genes or gene families, such as Plexins (PLXNA2, PLXNA4), Contactin5 (CNTN5), Sidekick2 (SDK2), and Cadherins (CDH8,11,12), are known to play crucial roles in establishing specific synaptic connections [50, 51, 52, 53, 32, 33, 54]. Others, particularly delta-protocadherins (PCDH7,9,11x), emerged as new candidates potentially mediating specific synaptic connections [3].

To elucidate the biological implications of these identified gene sets, we further conducted Gene Ontology (GO) enrichment analysis on the top genes through g:Profiler, a public web server for GO enrichment analysis [55, 56]. This tool allowed us to delve into the molecular functions, cellular pathways, and biological processes associated with these genes. Intriguingly, when we listed the top 10 significant GO terms for each latent dimension based on their adjusted p-values, we found two common themes: neuronal development and synaptic organization (Table S4). Table S4 also highlights the number of the top genes associated with each GO term, revealing that overall about 47% of these genes are involved in neural development and synaptic organization. Such findings underscore the potential roles of these genes in forming and shaping the specific connections between BC and RGC types.

6.2.4 Bilinear Model Predicts Connectivity Partners of Transcriptomically-Defined RGC Types

The success of recommendation systems in accurately predicting the preferences of new users inspired us to leverage the bilinear model for predicting the connectivity partners of RGC types whose interconnections with BC types remain uncharted. There are some RGC types defined from single-cell transcriptomic data [35], which lack clear correspondence with those identified through connectomics studies [36]. This discrepancy leaves the connectivity patterns of these transcriptionally-defined RGC types unknown, providing an opportunity for our model to predict their BC partners.

To accomplish this, we first projected these RGC types into the same latent space as those used to train the model (Figure 7a). We then employed this projection to construct a connectivity matrix

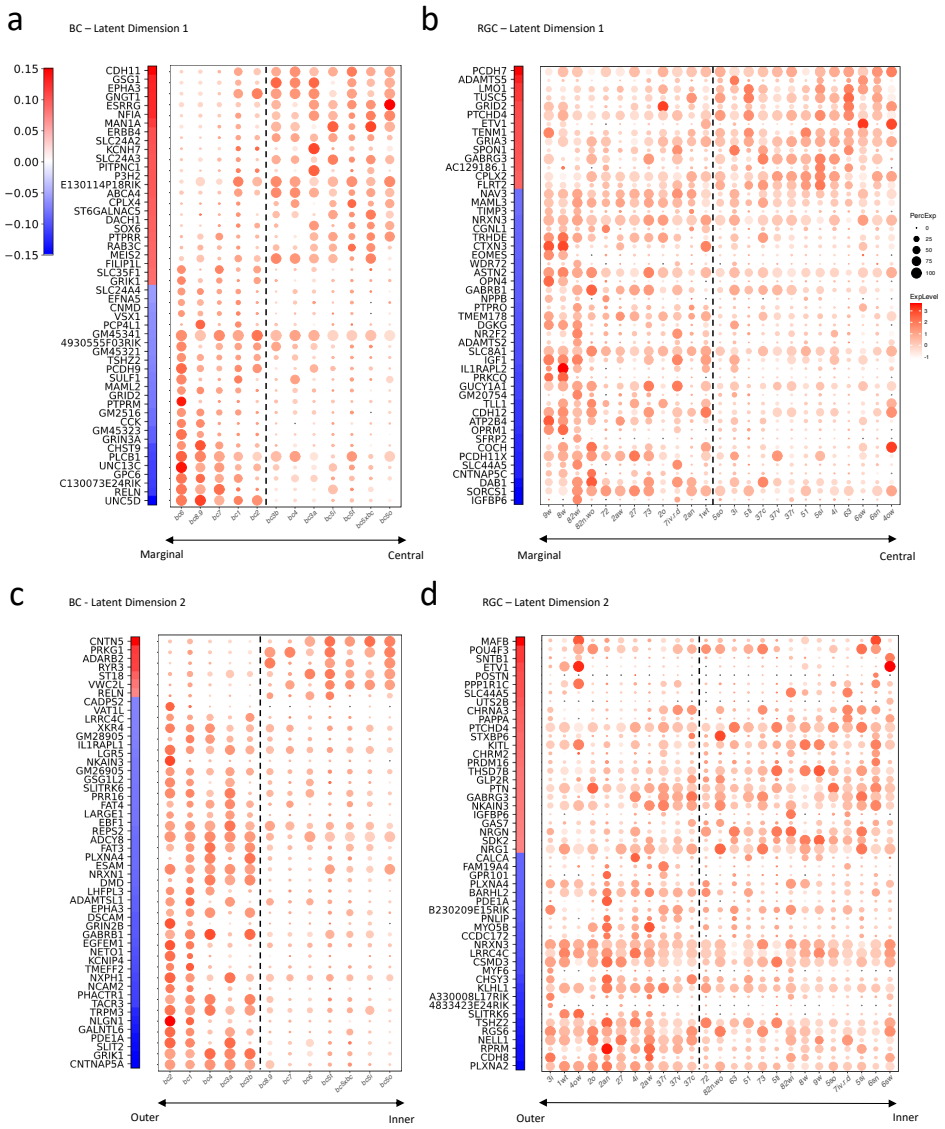

Figure 6: Gene signatures associated with the two latent dimensions. (a, b) Weight vectors of the top 50 genes for latent dimension 1, along with their expression patterns in BC types (a) and RGC types (b). The weight value is indicated in the color bar, with the sign represented by color (red: positive and blue: negative), and the magnitude by saturation. The expression pattern is represented by the size of each dot (indicating the percentage of cells expressing the gene) and the color saturation (representing the gene expression level). BC and RGC types are sorted by their positions along latent dimension 1, as shown in Figure 5c,f, with the dashed line separating the positive category from the negative category. (c, d) Weight vectors of the top 50 genes for latent dimension 2, and their expression patterns in BC types (c) and RGC types (d), depicted in the same manner as in (a) and (b). BC and RGC types are sorted by their positions along latent dimension 2.

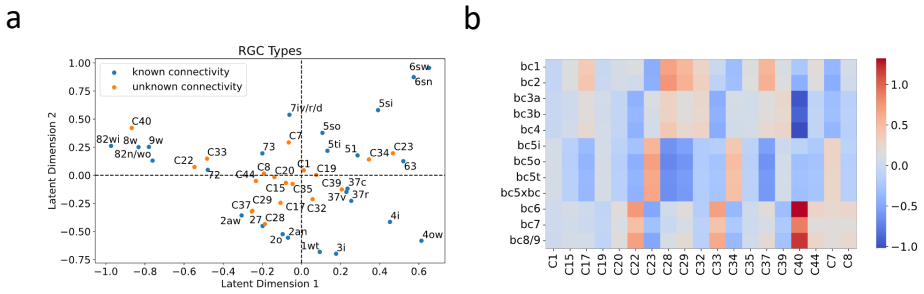

Figure 7: BC partner prediction of transcriptionally-defined RGC types. (a) Projection of transcriptionally-defined RGC types with unknown connectivity into the same latent space as those with known connectivity. (b) The resulting predicted connectivity matrix between these RGC types and BC types. Transcriptionally-defined RGC types are named according to Tran et al. [35]

between these RGC types and BC types (Figure 7b), facilitating educated estimates about their connectivity partners. For each transcriptionally-defined RGC type, we identified the top three BC types as potential partners, determined by the highest values present in the connectivity matrix. These three BC types could provide insight into the potential synaptic input to each RGC type. Detailed predictions are presented in Table S5.

Although the ground truth connectivity of these RGC types remains unknown due to the absence of matching types in connectomic data, Goetz et al. [38], via Patch-seq, attempted to match some transcriptomic types with functionally defined RGC types. These functional descriptions may hint at the BC partners of these RGC types. For instance, an RGC exhibiting OFF sustained responses is likely to be synaptically linked with BC types bc1-2, known to mediate OFF sustained pathways. Conversely, an RGC that displays ON sustained responses likely receives synaptic inputs from BC types bc6-9, which oversee ON sustained pathways. We summarized these functional descriptions in Table S5, referencing Figure 5A from Goetz et al. [38], and highlighted whether our predictions were consistent with these functional annotations. Among the ten predictions made, eight aligned with these functional descriptions, lending support to the predictive power of our model.

7 Discussion

7.1 Summary of Study

This study showcased a novel application of the bilinear modeling approach within the realm of gene expression analysis of neuronal type connectivity, drawing inspiration from recommendation systems - a machine learning domain focused on capturing intricate interactions between users and items and predicting user preferences. This analogy served as a useful framework in our study, where the roles of users and items in the recommendation systems are mirrored by presynaptic and postsynaptic neurons, respectively. Likewise, the user-item preference matrix corresponds to the synaptic connection matrix in neural circuits. The recommendation systems are based on the assumption that user preferences and item attributes can be represented by latent factors; similarly, our model assumes that synaptic connectivity between various neuron types is determined by a shared latent feature space derived from gene expression profiles.

The applicability and effectiveness of our bilinear model were validated using two different datasets. Applying it to the *C. elegans* neuronal dataset, which include data of gap junction connectivity and innexin expression at the individual neuron level, we showed that the model could be generalized to single-cell level connectivity by treating each neuronal type as an individual cell (Section 3.1), and incorporate spatial constraints such as physical contact between neurons into the weight matrix (Section 4.1). In a more complex scenario where the transcriptomic and connectomic data are from different sources and aligned at the neuronal-type level, we demonstrated the model's capability in

decoding the genetic underlying of the connectivity between neuronal types (Section 3.2), using the mouse retinal neuronal dataset (Section 4.2). This emphasizes the model's potential in offering insights into the genetic mechanisms that orchestrate synaptic connections across various nervous systems.

7.2 Insights from Analysis of *C. elegans* Dataset and Comparison with SCM

Using the *C. elegans* neuronal dataset, we conducted a comparative analysis between our bilinear model and the SCM, which correlates neuronal innexin expression with gap junction connectivity via a rule matrix [25, 26]. The SCM incorporates spatial constraints, such as physical contact between neurons, and represents the connectome as an edge list for regression against the Kronecker product of the gene expression matrix. Our model is closely related to the SCM, as it can be seen as factorization of the rule matrix into the product of two lower-dimensional transformation matrices. This factorization not only yielded a performance comparable to, if slightly better than, the SCM in reconstructing the gap junction connectivity matrix, but also revealing potential new innexin interactions for experimental exploration (Figure 2; Figure 3).

Beyond these, a crucial advantage of our bilinear model lies in in its computational efficiency, an attribute of significance when scaling to larger datasets, where the number of genes and the number of neurons or neuronal types escalates to the order of thousands, such as those of the mouse or macaque cortex [57, 58]. In such situation, the computational complexity of the SCM is substantial, given its reliance on the Kronecker product's dimensions and subsequent matrix inversion. In contrast, the computational demands of our bilinear model, driven primarily by matrix multiplication during gradient descent, are considerably more manageable, offering scalability and feasibility even as dataset sizes increase. Furthermore, the requirement to calculate the Kronecker product in SCM significantly heightens memory usage, critical when the data scale is large but memory resources are constrained. These advantages ensure our bilinear model a scalable solution when applied to other organisms and brain regions.

In assessing the bilinear model's and the SCM's performance to reconstruct *C. elegans* gap junction connectivity, the resulting modest ROC-AUC scores (approximately 0.64, much lower than the ideal 1.0) underscore the challenges in predicting electrical synapse specificity using innexion expressions alone. This suggests that additional molecular mechanisms, beyond innexin interactions, play crucial roles in forming specific electrical synaptic connections. Indeed, in the realm of chemical synapses, it's increasingly recognized that synaptic specificity is significantly influenced by factors such as cell-cell adhesion and recognition molecules, rather than just the pre- or post-synaptic machinery [3]. Recent studies support this viewpoint. For instance, research on the *C. elegans* motor circuit has revealed how a developmental program fine-tunes cAMP signaling to guide neuron-specific assembly of electrical synapses [59]. Furthermore, the observed coexistence of electrical and chemical synapses in close proximity intimates potential shared mechanisms underlying their specificity [60].

7.3 Insights from Application to Mouse Retinal Neuronal Dataset

Applying to the mouse retinal neuronal dataset, our bilinear model successfully reconstructed a neuronal type-specific connectivity map from gene expression profiles and recapitulated two core connectivity motifs of the retinal circuit, representing synapses formed in central or marginal parts of the IPL, and synapses formed in outer or inner regions (Figure 4; Figure 5). These motifs align well with recognized properties of retinal neurons: kinetic attributes (transient versus sustained responses) and polarity (ON versus OFF responses) [48, 11, 12, 49]. Significantly, these motifs aren't predefined or explicitly encoded into the model; instead, they emerge naturally from the model, further attesting to the model's power to capture key aspects of retinal circuitry.

The bilinear model also revealed unique insights into the gene signatures associated with the connectivity motifs. The weight vectors in the transformation matrices provide a means to assess the relative importance of individual genes. This direct interpretability is a significant advantage of the linear model, allowing for a more intuitive understanding of the gene-to-connectivity transformation process. Our analysis discovered distinct gene signatures associated with different connectivity motifs (Figure 6). Among these genes, some have been previously implicated in mediating specific synaptic connections, thererby validating our approach. For instance, Plexins A4 and A2 (PLXNA4, PLXNA2), predicted to be crucial for RGCs' synapsing in the outer IPL, have been shown to be

necessary for forming specific lamina of the IPL in the mouse retina, interacting with the guidance molecule Semaphorin 6A (SEM6A) [50, 51]. Contactin5 (CNTN5), which our model predicted as vital for BCs forming synapses in the inner IPL, has been shown to be essential for synapses between ON BCs and the ON lamina of ON-OFF direction-selective ganglion cells (ooDSGCs) [52]. Sidekick2 (SDK2), predicted to be critical for RGCs' synapses in the inner IPL, has been shown to guide the formation of a retinal circuit that detects differential motion [53]. Similarly, Cadherins (CDH8,11,12), whose combinations have been implicated in synaptic specificity within retinal circuits [32, 33], were highlighted for multiple connectivity motifs. In particular, Cadherin8 (CDH8), which our model predicted to be crucial for RGC's synaptic connections in the outer IPL, has been shown to be guided by the transciptional factor Tbr1 for laminar patterning of J-RGCs, a type of OFF direction-selective RGCs [54]. In addition to these validated gene signatures, our analysis identified promising candidate genes that may mediate specific synaptic connections. Particularly, delta-protocadherins (PCDH7,9,11x) appeared as potential new candidates. While their roles in synaptic connectivity aren't fully understood [3], mutations in delta-protocadherins in mice and humans have been linked with various neurological phenotypes, including axon growth and guidance impairments and changes in synaptic plasticity and stability [61, 62, 63, 64]. Future experimental studies are needed to validate these findings and further unravel the roles of these genes in neural circuit formation and function in the mouse retina.

The bilinear model's utility extends beyond the identification of gene signatures, emerging as a potent tool for hypothesis generation, particularly in predicting connectivity for transcriptionally-defined neuronal types whose synaptic partners remain uncharted (Figure 7). Trained on data from a specific neural region, the bilinear model can facilitate the anticipation of synaptic partners for newly characterized transcriptional types within that region, thereby generating hypotheses on their functional roles within neural circuits. Furthermore, this model opens avenues for inferring neural wiring alterations resulting from genetic manipulations. For instance, by altering the genetic profile of certain neuronal types to create new transcriptionally defined types, we can use the model to predict changes in their synaptic partners, offering insights into the consequent reconfiguration of neural networks. This could be further extended to hypothesize the rewiring of the brain under psychological disorders, such as autism, where significant connectome changes suggest shifts in synaptic partner choices [65, 66]. With recent availability of neuronal gene expression data of autism [67, 68, 69], our model stands poised to predict the implications of such genetic profiles on neural circuitry, guiding the research of understanding and treating this psychological disorder.

While our bilinear model offers valuable insights into the connectivity motifs of retinal circuits and the associated gene signatures, with many findings aligning with existing literature, it is important to acknowledge certain limitations of this study. Firstly, the model's connectivity matrix was deduced from stratification profiles derived from EM reconstruction. Although prior research has indicated stratification as a meaningful indicator of connectivity within the mouse retina, as certain BC types preferentially connect with specific RGC types stratified in the same lamina [32, 53, 33], this metric may not capture the entire complexity of synaptic connections [70]. The incorporation of additional experimental data, such as electrophysiological measurements, could enhance both the accuracy and the reliability of the connectivity metrics. Secondly, the model, despite its overall success in reconstructing the connectivity matrix, missed several connections, notably among specific BC-RGC pairs such as those between RGC types 51, 5ti and BC types 3a, 3b, and 4 (Figure S5). This highlights the potential for a more complex approach, such as deep learning models, to capture the subtleties of synaptic connections. Finally, the list of top genes identified by our model is enriched with genes directly mediating synapse formation and maintenance, such as adhesion molecules (Figure 6; Table S4), yet overlooks transcription factors like Tbr1 known to affect synaptic specificity [54]. These factors, impacting various neuronal functionalities, might not be captured by a linear model that inherently favors predictor variables that strongly correlate with the target variable.

8 Future Directions

8.1 Experiment Validation of Candidate Genes

The bilinear model enables the predictions of possible changes in synaptic connections resulting from changes in expressions of the candidate genes. Emerging genome editing technologies, particularly CRISPR/Cas9 [71, 72], offers a precise and efficient way to validate these predictions through experiments. By leveraging CRISPR/Cas9, targeted genetic manipulations, such as gene silencing or

modification, can be conducted to assess their impact on synaptic connectivity. In the context of the mouse retina, the delivery of CRISPR/Cas9 components into BCs or RGCs can be achieved through electroporation or adeno-associated virus (AAV) vectors, respectively, allowing for targeted gene intervention [73, 74].

The finding of delta-protocadherins (PCDH7, 9, 11x) as potential mediators of synaptic specificity in the mouse retina presents an exciting opportunity for experimental exploration. We propose to design CRISPR/Cas9 systems targeting these delta-protocadherins (PCDH7,9,11x), similar to those detailed in a recent study [75]. Delivered to the mouse retina using AAV vectors, we expect to knockdown delta-protocadherin expressions in RGCs [74]. With PCDH7 identified as a key factor in synapse formation within the central regions of the IPL, a focal point of our investigation will be RGC types like W3B RGCs, which are known to stratify in these central layers [76]. The consequences of PCDH7 downregulation on the connectivity of W3B RGCs can be examined through multiple approaches [53]: immunohistochemical techniques or the use of transgenic markers can reveal morphological changes indicative of altered connectivity; electrophysiological assessments, such as targeted recordings from postsynaptic neurons while optogenetically stimulating presynaptic partners, offer a functional probe into the synaptic alterations. Similarly, as PCDH9 and PCDH11x are implicated in synaptic connections within the marginal regions of the IPL, candidate RGCs for examination could include ON and OFF sustained alpha RGCs, known for their peripheral stratifications [77].

This experimental paradigm is not confined to the mouse retina but extends to a broad range of neuronal circuits, thanks to the flexibility and wide applicability of genome editing tools like CRISPR/Cas9 [78, 79, 80]. The capacity to induce targeted gene knockouts or modifications will empower researchers to validate our bilinear model's predictions and explore the underlying genetic mechanisms for synaptic formation and maintenance. This endeavor opens new avenues for deciphering the complex interplay between genetics and neural circuit wiring, furthering our comprehension of the molecular mechanisms driving synaptic specificity.

8.2 Application to Other Neural Systems

Our bilinear model, while illustrated using the *C. elegans* and mouse retina datasets, holds significant potential for elucidating the genetic underpinnings of neuronal connectivity across various species and brain regions, contingent upon the availability of comprehensive gene expression profiles and synaptic connection data. For instance, the advent of a comprehensive single-cell transcriptome atlas for the adult fruit fly brain, alongside the recent establishment of its complete connectome, offers a fertile ground for extending our model to decipher the complex neural circuits of *Drosophila* [81, 82].

In the context of the mouse brain, the depth and breadth of single-cell sequencing efforts have unveiled a rich tapestry of transcriptomic cell types across cortex regions and the hippocampus [83, 84, 85, 57]. These efforts, in tandem with connectomic studies that meticulously map neuronal connections, lay a foundation for integrating transcriptomic and connectomic data [86, 87, 46, 88]. Such integration, especially across diverse brain regions, presents an exciting avenue to uncover both neuronal connection mechanisms that are shared by neuronal types across different regions and those unique to specific regions. The scalability of our bilinear model, akin to collaborative filtering's effectiveness in commercial domains, supports the prospect of its cross-regional application. This approach positions our model at the forefront of efforts to explore how gene expression patterns contribute to the diversity of neuronal circuits across brain areas, moving us closer to a holistic understanding of the genetic blueprint of neuronal connectivity throughout the entire brain.

Nevertheless, we recognize the challenge that such well-aligned connectomic and transcriptomic data may not always be readily available. To address this, future research endeavors will also explore adaptations of our model to other available datasets, such as those that combine single-cell transcriptomic profiling with long-range neuronal projection mapping [89, 90]. Furthermore, our model is amenable to integration with trans-synaptic tracer-based sequencing methods [91, 92], expanding its utility in studies where detailed connectomic information is limited. Pursuing these avenues is pivotal in broadening the model's utility and ensuring its relevance across a wider spectrum of brain connectivity research, making it an invaluable tool in the quest to unravel the complexities of neural circuitry.

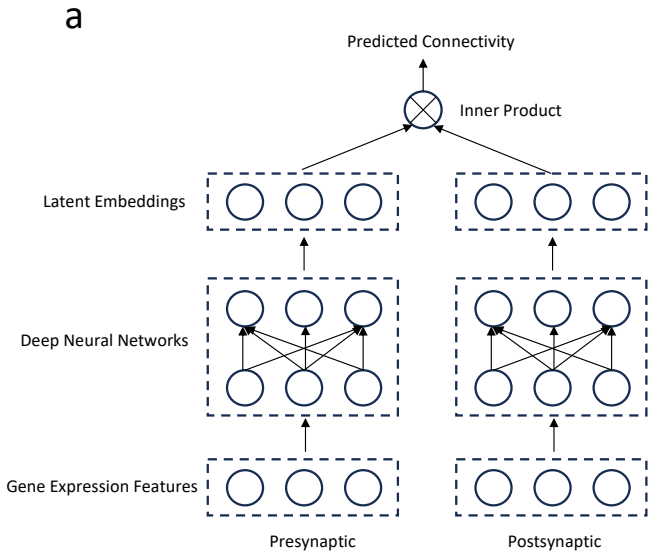

Figure 8: Future direction: A two-tower deep learning model. (a) Gene expression profiles of pre- and post-synaptic neurons are transformed into latent embedding representations via deep neural networks. The connectivity metric between the pre- and post-synaptic neurons is predicted by taking the inner product of their respective latent embeddings.

8.3 Model Advancements

To enhance the model's fidelity and applicability, we propose several advancements. First, we advocate for the integration of auxiliary data types, including electrophysiological data, neuron tracing data, and an array of omics data such as proteomics and epigenetics data, to augment and enrich the model's training base [49, 91, 92, 93, 94]. These data modalities offer complementary insights into neuronal function and connectivity, providing valuable context that can inform and refine the model's predictions.

Second, we envision extending the bilinear model to incorporate non-linear interactions, capturing the intricate dynamics between gene expressions and synaptic connections. A potential pathway for this is through kernel methods or the integration of neural networks, specifically adopting the "two-tower model" framework renowned in modern recommendation systems (Figure 8). In this model, each "tower" is a deep neural network that undertakes the non-linear transformation of input features [95, 96]. This architecture has proven effective in capturing complex user-item interactions and could significantly enhance our model's ability to decipher the nuanced relationships between genetics and neural connectivity.

9 Data and Code Availability

Pointers to the data used in this study and the source code of the bilinear model are available at https://github.com/muqiao0626/Bilinear_Model.

10 Supplementary Materials

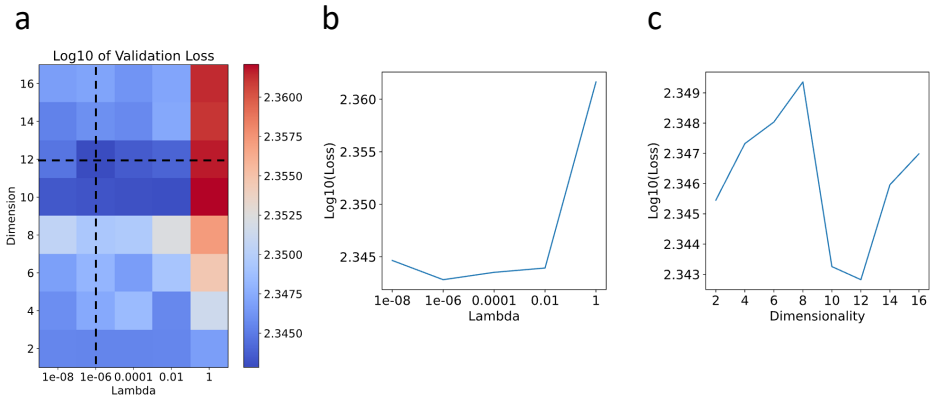

Supplementary Figure S1: Hyperparameter selection through cross-validation for the *C. elegans* neuronal dataset. (a) Heatmap plot of the logarithm (base 10) of the validation loss, showing variations with respect to λ across [10^{-8}, 10^{-6}, 0.0001, 0.01, 1] and dimensionality across [2, 4, 6, 8, 10, 12, 14, 16]. (b) Plot showing the logarithm (base 10) of the validation loss against λ over the range [10^{-8}, 10^{-6}, 0.0001, 0.01, 1]. (c) Plot displaying the logarithm (base 10) of the validation loss against dimensionality over the range [2, 4, 6, 8, 10, 12, 14, 16].

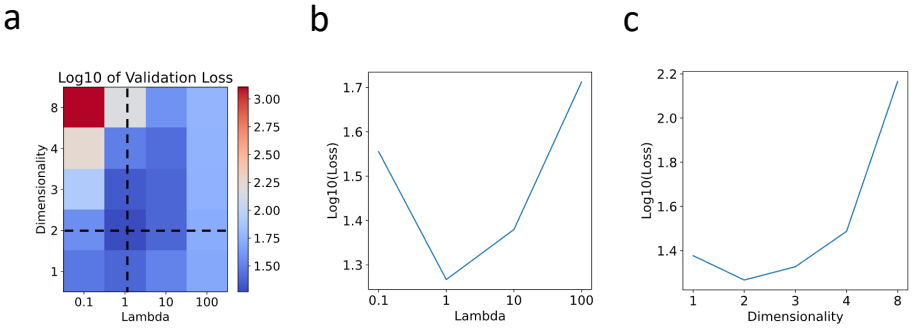

Supplementary Figure S2: Hyperparameter selection through cross-validation for the mouse retinal neuronal dataset. (a) Heatmap plot of the logarithm (base 10) of the validation loss, showing variations with respect to λ across [0.1, 1, 10, 100] and dimensionality across [1, 2, 3, 4, 8]. (b) Plot showing the logarithm (base 10) of the validation loss against λ over the range [0.1, 1, 10, 100]. (c) Plot displaying the logarithm (base 10) of the validation loss against dimensionality over the range [1, 2, 3, 4, 8].

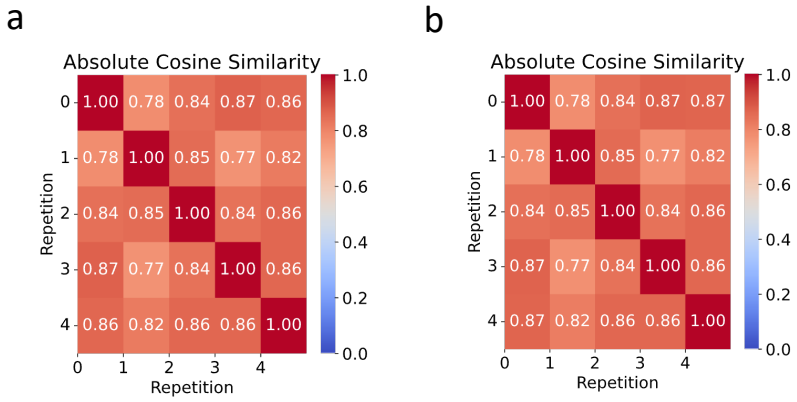

Supplementary Figure S3: Heatmaps showcasing the average absolute cosine similarities across five optimization repetitions for (a) $\hat{\boldsymbol{A}}$ and (b) $\hat{\boldsymbol{B}}$. The color scale reflects value of the metric.

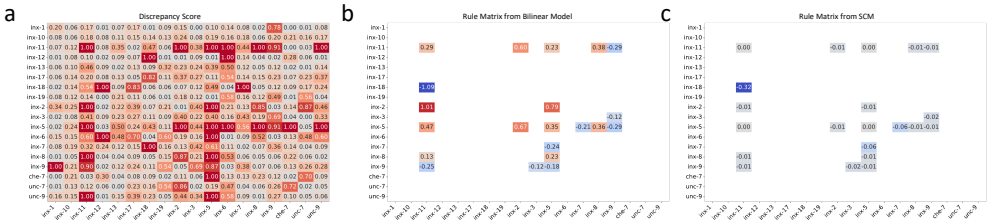

Supplementary Figure S4: Detailed discrepancy analysis between the bilinear model and SCM genetic rules. (a) Discrepancy scores (DS) identifying divergences between the models' rule matrices. (b, c) Significant entries from the bilinear model's rule matrix (b) and the SCM's rule matrix (c), respectively, with DS exceeding 0.5 and matrix entries no less than 0.1.

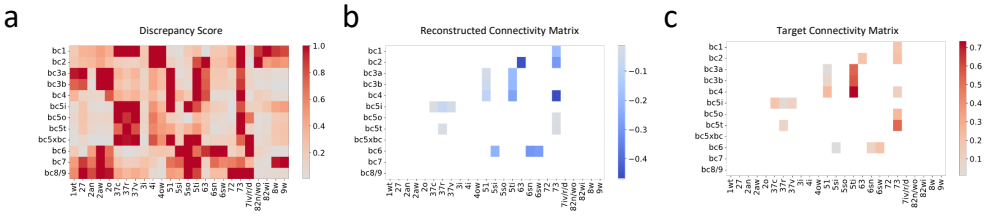

Supplementary Figure S5: Detailed discrepancy analysis between the reconstructed and the target connectivity matrices. (a) Discrepancy scores (DS) identifying divergences between the two matrices. (b, c) Specific connections present in the target matrix (c) that were not captured in the reconstructed matrix (b), with DS exceeding 0.5, indicating notable deviations.

Supplementary Table S1: Correspondence of Mouse BC types [37, 34]

Shekhar et al. 2016	**Greene et al. 2016**
BC1a, BC1b	bc1
BC2	bc2
BC3a	bc3a
BC4	bc4
BC5a	bc5i
BC5b	bc5o
BC5c	bc5t
BC5d	(bc5)xbc
BC6	bc6
BC7	bc7
BC8, BC9	bc8/9

Supplementary Table S2: Correspondence of Mouse RGC types [36, 35, 38]

Goetz et al. (2022) Type	**Bae et al. (2018) Eyewire type**	**Tran et al. (2019) Cluster**
ON sus alpha	8w	C43
OFFhOS	2aw	C9
OFFvOS	2aw	C5
ON tr SmRF	6sn	C30
OFF tr alpha	4ow	C45
OFF tr SmRF	4i	C21
ONhOS SmRF	82wi	C27
ONhOS LgRF	82n/wo	C36
ONvOS SmRF	72	C38
ON DS sus DN	7iv	C10
ON DS sus T	7ir	C10
ON DS sus V	7id	C10
OODS D	37v	C16
OODS T	37r	C24
HD1	5si	C13
HD2	5so	C6
UHD	5ti	C2
LED	51	C11
F-mini-ON	63	C3
ON delayed	73	C14
ON bursty	3i	C18
bSbC	2o	C25
sSbC EW27	27	C26

Supplementary Table S3: Correspondence of Mouse RGC types [36, 35, 38]

Goetz et al. (2022) Type	**Bae et al. (2018) Eyewire type**	**Tran et al. (2019) Cluster**
M2	9w	C31
OFF sus alpha	1wt	C42
OODS N	37c	C12
F-mini-OFF	2an	C4
ON tr alpha	6sw	C41

Supplementary Table S4: Gene Ontology (GO) Terms Associated with Latent Dimensions in BCs and RGCs

Term Name	Term ID	Adjusted P-value	Number of Genes
BC Latent Dimension 1			
modulation of chemical synaptic transmission	GO:0050804	0.000440326	9
regulation of trans-synaptic signaling	GO:0099177	0.000445672	9
synaptic signaling	GO:0099536	0.000504129	10
nervous system development	GO:0007399	0.000591482	15
neuron differentiation	GO:0030182	0.000776891	12
generation of neurons	GO:0048699	0.001293397	12
cell-cell adhesion via plasma-membrane adhesion molecules	GO:0098742	0.003255938	6
chemical synaptic transmission	GO:0007268	0.003529887	9
anterograde trans-synaptic signaling	GO:0098916	0.003529887	9
trans-synaptic signaling	GO:0099537	0.003763337	9
RGC Latent Dimension 1			
system development	GO:0048731	1.14E-05	21
nervous system development	GO:0007399	1.53E-05	17
anatomical structure development	GO:0048856	1.67E-05	25
synapse	GO:0045202	3.22E-05	13
somatodendritic compartment	GO:0036477	3.61E-05	11
multicellular organism development	GO:0007275	3.76E-05	22
synaptic membrane	GO:0097060	4.90E-05	8
postsynaptic membrane	GO:0045211	5.92E-05	7
neurogenesis	GO:0022008	0.000126449	14
developmental process	GO:0032502	0.000135356	25
BC Latent Dimension 2			
neuron differentiation	GO:0030182	1.07E-08	17
generation of neurons	GO:0048699	2.28E-08	17
neuron development	GO:0048666	9.30E-08	15
neurogenesis	GO:0022008	1.98E-07	17
neuron projection development	GO:0031175	2.18E-07	14
cell adhesion	GO:0007155	7.00E-07	15
synaptic membrane	GO:0097060	6.20E-06	9
cell periphery	GO:0071944	8.75E-06	27
plasma membrane	GO:0005886	1.07E-05	26
nervous system development	GO:0007399	2.36E-05	17
RGC Latent Dimension 2			
neuron projection development	GO:0031175	0.00289625	10
nervous system development	GO:0007399	0.00563224	14
neuron projection morphogenesis	GO:0048812	0.0067497	8
neurogenesis	GO:0022008	0.00734347	12
plasma membrane bounded cell projection morphogenesis	GO:0120039	0.00789142	8
neuron differentiation	GO:0030182	0.00817177	11
cell projection morphogenesis	GO:0048858	0.008392	8
neuron development	GO:0048666	0.00937721	10
synaptic membrane	GO:0097060	0.00944134	6
cell part morphogenesis	GO:0032990	0.01143062	8

Supplementary Table S5: Predicted BC Partners of Transciptionally-defined RGC Types

Tran et al. (2019)	Predicted BC Partners	Based on Goetz et al. (2022) Figure 5A	Consistent
C1: W3L1	bc5o, bc5xbc, bc5t	Match to 6 functional types	-
C15	bc2, bc1, bc8/9	-	-
C17	bc2, bc1, bc4	-	-
C19	bc5o, bc5xbc, bc5t	"HD2" like: Between SAC bands	Yes
C20	bc6, bc8/9, bc7	-	-
C22: MX	bc6, bc8/9, bc7	"M2" like: ON, Sustained	Yes
C23: W3D2	bc5o, bc5xbc, bc5t	"OFF tr alpha" like: OFF, Transient	No
C28: F-midi-OFF	bc2, bc1, bc4	Match to 3 functional types	-
C29	bc2, bc1, bc4	"OFF sus alpha" like: OFF, Sustained	Yes
C32	bc2, bc4, bc1	Match to 2 functional types	-
C33: M1a	bc6, bc8/9, bc7	"M2" like: ON, Sustained	Yes
C34	bc5o, bc5xbc, bc5t	"ON tr MeRF" like: ON, Transient	Yes
C35	bc2, bc1, bc4	Match to 4 functional types	-
C37	bc2, bc1, bc4	"OFF tr MeRF" like: OFF, Transient	Yes
C39	bc4, bc3a, bc3b	-	-
C40: M1b	bc6, bc8/9, bc7	"M1": ON, Sustained	Yes
C44	bc6, bc8/9, bc7	"LED" like: Between SAC bands	No
C7	bc5o, bc5i, bc5xbc	-	-
C8	bc6, bc8/9, bc7	"PixON" like: ON, Sustained	Yes

References

[1] Sebastian Seung. *Connectome: How the Brain's Wiring Makes Us Who We Are*. Houghton Mifflin Harcourt, 2012.

[2] F. Polleux and William Snider. Initiating and growing an axon. *Cold Spring Harb Perspect Biol*, 2(4):a001925, April 2010.

[3] Joshua R. Sanes and S. Lawrence Zipursky. Synaptic Specificity, Recognition Molecules, and Assembly of Neural Circuits. *Cell*, 181(6):1434–1435, June 2020.

[4] Hongkui Zeng and Joshua R. Sanes. Neuronal cell-type classification: Challenges, opportunities and the path forward. *Nat Rev Neurosci*, 18(9):530–546, September 2017.

[5] Oliver Stegle, Sarah A. Teichmann, and John C. Marioni. Computational and analytical challenges in single-cell transcriptomics. *Nat Rev Genet*, 16(3):133–145, March 2015.

[6] Winfried Denk and Heinz Horstmann. Serial Block-Face Scanning Electron Microscopy to Reconstruct Three-Dimensional Tissue Nanostructure. *PLOS Biology*, 2(11):e329, October 2004.

[7] Moritz Helmstaedter, Kevin L. Briggman, Srinivas C. Turaga, Viren Jain, H. Sebastian Seung, and Winfried Denk. Connectomic reconstruction of the inner plexiform layer in the mouse retina. *Nature*, 500(7461):168–174, August 2013.

[8] Juan Carlos Tapia, Narayanan Kasthuri, Kenneth J. Hayworth, Richard Schalek, Jeff W. Lichtman, Stephen J. Smith, and JoAnn Buchanan. High-contrast en bloc staining of neuronal tissue for field emission scanning electron microscopy. *Nat Protoc*, 7(2):193–206, February 2012.

[9] Yehuda Koren, Robert Bell, and Chris Volinsky. Matrix Factorization Techniques for Recommender Systems. *Computer*, 42(8):30–37, August 2009.

[10] E. Anne Martin, Abagael M. Lasseigne, and Adam C. Miller. Understanding the Molecular and Cell Biological Mechanisms of Electrical Synapse Formation. *Front Neuroanat*, 14:12, April 2020.

[11] Thomas Euler, Silke Haverkamp, Timm Schubert, and Tom Baden. Retinal bipolar cells: Elementary building blocks of vision. *Nat Rev Neurosci*, 15(8):507–519, August 2014.

[12] Joshua R. Sanes and Richard H. Masland. The Types of Retinal Ganglion Cells: Current Status and Implications for Neuronal Classification. *Annual Review of Neuroscience*, 38(1):221–246, 2015.

[13] Tim Gollisch and Markus Meister. Eye smarter than scientists believed: Neural computations in circuits of the retina. *Neuron*, 65(2):150–164, January 2010.

[14] Rava Azeredo da Silveira and Botond Roska. Cell types, circuits, computation. *Curr Opin Neurobiol*, 21(5):664–671, October 2011.

[15] Nalin M. Kumar and Norton B. Gilula. The Gap Junction Communication Channel. *Cell*, 84(3):381–388, February 1996.

[16] Pauline Phelan, Jonathan P. Bacon, Jane A. Davies, Lucy A. Stebbings, and Martin G. Todman. Innexins: A family of invertebrate gap-junction proteins. *Trends in Genetics*, 14(9):348–349, September 1998.

[17] Ithai Rabinowitch and William R Schafer. Engineering new synaptic connections in the C. elegans connectome. *Worm*, 4(2):e992668, January 2015.

[18] Gary Marcus, Adam Marblestone, and Thomas Dean. The atoms of neural computation. *Science*, 346(6209):551–552, October 2014.

[19] Thomas C. Südhof. Synaptic Neurexin Complexes: A Molecular Code for the Logic of Neural Circuits. *Cell*, 171(4):745–769, November 2017.

[20] David H. Hall. Gap junctions in C. elegans: Their roles in behavior and development. *Dev Neurobiol*, 77(5):587–596, May 2017.

[21] Joris de Wit and Anirvan Ghosh. Specification of synaptic connectivity by cell surface interactions. *Nat Rev Neurosci*, 17(1):22–35, January 2016.

[22] Alex Fornito, Aurina Arnatkevičiūtė, and Ben D. Fulcher. Bridging the Gap between Connectome and Transcriptome. *Trends Cogn Sci*, 23(1):34–50, January 2019.

[23] Alon Kaufman, Gideon Dror, Isaac Meilijson, and Eytan Ruppin. Gene Expression of Caenorhabditis elegans Neurons Carries Information on Their Synaptic Connectivity. *PLoS Comput Biol*, 2(12):e167, December 2006.

[24] Vinay Varadan, David M. Miller, and Dimitris Anastassiou. Computational inference of the molecular logic for synaptic connectivity in C. elegans. *Bioinformatics*, 22(14):e497–506, July 2006.

[25] István A. Kovács, Dániel L. Barabási, and Albert-László Barabási. Uncovering the genetic blueprint of the C. elegans nervous system. *Proceedings of the National Academy of Sciences*, 117(52):33570–33577, December 2020.

[26] Dániel L. Barabási and Albert-László Barabási. A Genetic Model of the Connectome. *Neuron*, 105(3):435–445.e5, February 2020.

[27] Seth R. Taylor, Gabriel Santpere, Alexis Weinreb, Alec Barrett, Molly B. Reilly, Chuan Xu, Erdem Varol, Panos Oikonomou, Lori Glenwinkel, Rebecca McWhirter, Abigail Poff, Manasa Basavaraju, Ibnul Rafi, Eviatar Yemini, Steven J. Cook, Alexander Abrams, Berta Vidal, Cyril Cros, Saeed Tavazoie, Nenad Sestan, Marc Hammarlund, Oliver Hobert, and David M. Miller. Molecular topography of an entire nervous system. *Cell*, 184(16):4329–4347.e23, August 2021.

[28] Hongkui Zeng. What is a cell type and how to define it? *Cell*, 185(15):2739–2755, July 2022.

[29] Francesco Ricci, Lior Rokach, and Bracha Shapira. Introduction to Recommender Systems Handbook. In Francesco Ricci, Lior Rokach, Bracha Shapira, and Paul B. Kantor, editors, *Recommender Systems Handbook*, pages 1–35. Springer US, Boston, MA, 2011.

[30] Xiaoyuan Su and Taghi M. Khoshgoftaar. A Survey of Collaborative Filtering Techniques. *Advances in Artificial Intelligence*, 2009:e421425, October 2009.

[31] Steffen Rendle, Christoph Freudenthaler, Zeno Gantner, and Lars Schmidt-Thieme. BPR: Bayesian Personalized Ranking from Implicit Feedback, May 2012. Comment: Appears in Proceedings of the Twenty-Fifth Conference on Uncertainty in Artificial Intelligence (UAI2009).

[32] Xin Duan, Arjun Krishnaswamy, Irina De la Huerta, and Joshua R. Sanes. Type II cadherins guide assembly of a direction-selective retinal circuit. *Cell*, 158(4):793–807, August 2014.

[33] Xin Duan, Arjun Krishnaswamy, Mallory A. Laboulaye, Jinyue Liu, Yi-Rong Peng, Masahito Yamagata, Kenichi Toma, and Joshua R. Sanes. Cadherin Combinations Recruit Dendrites of Distinct Retinal Neurons to a Shared Interneuronal Scaffold. *Neuron*, 99(6):1145–1154.e6, September 2018.

[34] Karthik Shekhar, Sylvain W. Lapan, Irene E. Whitney, Nicholas M. Tran, Evan Z. Macosko, Monika Kowalczyk, Xian Adiconis, Joshua Z. Levin, James Nemesh, Melissa Goldman, Steven A. McCarroll, Constance L. Cepko, Aviv Regev, and Joshua R. Sanes. COMPREHENSIVE CLASSIFICATION OF RETINAL BIPOLAR NEURONS BY SINGLE-CELL TRANSCRIPTOMICS. *Cell*, 166(5):1308–1323.e30, August 2016.

[35] Nicholas M. Tran, Karthik Shekhar, Irene E. Whitney, Anne Jacobi, Inbal Benhar, Guosong Hong, Wenjun Yan, Xian Adiconis, McKinzie E. Arnold, Jung Min Lee, Joshua Z. Levin, Dingchang Lin, Chen Wang, Charles M. Lieber, Aviv Regev, Zhigang He, and Joshua R. Sanes. Single-cell profiles of retinal neurons differing in resilience to injury reveal neuroprotective genes. *bioRxiv*, page 711762, July 2019.

[36] J. Alexander Bae, Shang Mu, Jinseop S. Kim, Nicholas L. Turner, Ignacio Tartavull, Nico Kemnitz, Chris S. Jordan, Alex D. Norton, William M. Silversmith, Rachel Prentki, Marissa Sorek, Celia David, Devon L. Jones, Doug Bland, Amy L. R. Sterling, Jungman Park, Kevin L. Briggman, H. Sebastian Seung, and Eyewirers. Digital Museum of Retinal Ganglion Cells with Dense Anatomy and Physiology. *Cell*, 173(5):1293–1306.e19, May 2018.

[37] Matthew J. Greene, Jinseop S. Kim, H. Sebastian Seung, and EyeWirers. Analogous Convergence of Sustained and Transient Inputs in Parallel On and Off Pathways for Retinal Motion Computation. *Cell Rep*, 14(8):1892–1900, March 2016.

[38] Jillian Goetz, Zachary F. Jessen, Anne Jacobi, Adam Mani, Sam Cooler, Devon Greer, Sabah Kadri, Jeremy Segal, Karthik Shekhar, Joshua R. Sanes, and Gregory W. Schwartz. Unified classification of mouse retinal ganglion cells using function, morphology, and gene expression. *Cell Rep*, 40(2):111040, July 2022.

[39] Andrew Butler, Paul Hoffman, Peter Smibert, Efthymia Papalexi, and Rahul Satija. Integrating single-cell transcriptomic data across different conditions, technologies, and species. *Nat Biotechnol*, 36(5):411–420, June 2018.

[40] Tim Stuart, Andrew Butler, Paul Hoffman, Christoph Hafemeister, Efthymia Papalexi, William M. Mauck, Yuhan Hao, Marlon Stoeckius, Peter Smibert, and Rahul Satija. Comprehensive Integration of Single-Cell Data. *Cell*, 177(7):1888–1902.e21, June 2019.

[41] Steven J. Cook, Travis A. Jarrell, Christopher A. Brittin, Yi Wang, Adam E. Bloniarz, Maksim A. Yakovlev, Ken C. Q. Nguyen, Leo T.-H. Tang, Emily A. Bayer, Janet S. Duerr, Hannes E. Bülow, Oliver Hobert, David H. Hall, and Scott W. Emmons. Whole-animal connectomes of both Caenorhabditis elegans sexes. *Nature*, 571(7763):63–71, July 2019.

[42] Mu Qiao. Factorized Discriminant Analysis for Genetic Signatures of Neuronal Phenotypes. *arXiv preprint arXiv:2010.02171*, November 2023.

[43] Hung-I. Harry Chen, Yufang Jin, Yufei Huang, and Yidong Chen. Detection of high variability in gene expression from single-cell RNA-seq profiling. *BMC Genomics*, 17 Suppl 7:508, August 2016.

[44] Shristi Pandey, Karthik Shekhar, Aviv Regev, and Alexander F. Schier. Comprehensive Identification and Spatial Mapping of Habenular Neuronal Types Using Single-Cell RNA-Seq. *Curr. Biol.*, 28(7):1052–1065.e7, April 2018.

[45] Yerbol Z Kurmangaliyev, Juyoun Yoo, Samuel A LoCascio, and S Lawrence Zipursky. Modular transcriptional programs separately define axon and dendrite connectivity. *eLife*, 8:e50822, November 2019.

[46] Nicholas L. Turner, Thomas Macrina, J. Alexander Bae, Runzhe Yang, Alyssa M. Wilson, Casey Schneider-Mizell, Kisuk Lee, Ran Lu, Jingpeng Wu, Agnes L. Bodor, Adam A. Bleckert, Derrick Brittain, Emmanouil Froudarakis, Sven Dorkenwald, Forrest Collman, Nico Kemnitz, Dodam Ih, William M. Silversmith, Jonathan Zung, Aleksandar Zlateski, Ignacio Tartavull, Szi-chieh Yu, Sergiy Popovych, Shang Mu, William Wong, Chris S. Jordan, Manuel Castro, JoAnn Buchanan, Daniel J. Bumbarger, Marc Takeno, Russel Torres, Gayathri Mahalingam, Leila Elabbady, Yang Li, Erick Cobos, Pengcheng Zhou, Shelby Suckow, Lynne Becker, Liam Paninski, Franck Polleux, Jacob Reimer, Andreas S. Tolias, R. Clay Reid, Nuno Maçarico da Costa, and H. Sebastian Seung. Reconstruction of neocortex: Organelles, compartments, cells, circuits, and activity. *Cell*, 185(6):1082–1100.e24, March 2022.

[47] Jinseop S. Kim, Matthew J. Greene, Aleksandar Zlateski, Kisuk Lee, Mark Richardson, Srinivas C. Turaga, Michael Purcaro, Matthew Balkam, Amy Robinson, Bardia F. Behabadi, Michael Campos, Winfried Denk, and H. Sebastian Seung. Space–time wiring specificity supports direction selectivity in the retina. *Nature*, 509(7500):331–336, May 2014.

[48] Richard H. Masland. The Neuronal Organization of the Retina. *Neuron*, 76(2):266–280, October 2012.

[49] Tom Baden, Philipp Berens, Katrin Franke, Miroslav Román Rosón, Matthias Bethge, and Thomas Euler. The functional diversity of retinal ganglion cells in the mouse. *Nature*, 529(7586):345–350, January 2016.

[50] Ryota L. Matsuoka, Kim T. Nguyen-Ba-Charvet, Aijaz Parray, Tudor C. Badea, Alain Chédotal, and Alex L. Kolodkin. Transmembrane semaphorin signalling controls laminar stratification in the mammalian retina. *Nature*, 470(7333):259–263, February 2011.

[51] Lu O. Sun, Zheng Jiang, Michal Rivlin-Etzion, Randal Hand, Colleen M. Brady, Ryota L. Matsuoka, King-Wai Yau, Marla B. Feller, and Alex L. Kolodkin. On and off retinal circuit assembly by divergent molecular mechanisms. *Science*, 342(6158):1241974, November 2013.

[52] Yi-Rong Peng, Nicholas M. Tran, Arjun Krishnaswamy, Dimitar Kostadinov, Emily M. Martersteck, and Joshua R. Sanes. Satb1 Regulates Contactin 5 to Pattern Dendrites of a Mammalian Retinal Ganglion Cell. *Neuron*, 95(4):869–883.e6, August 2017.

[53] Arjun Krishnaswamy, Masahito Yamagata, Xin Duan, Y. Kate Hong, and Joshua R. Sanes. Sidekick 2 directs formation of a retinal circuit that detects differential motion. *Nature*, 524(7566):466–470, August 2015.

[54] Jinyue Liu, Jasmine D. S. Reggiani, Mallory A. Laboulaye, Shristi Pandey, Bin Chen, John L. R. Rubenstein, Arjun Krishnaswamy, and Joshua R. Sanes. Tbr1 instructs laminar patterning of retinal ganglion cell dendrites. *Nat Neurosci*, 21(5):659–670, May 2018.

[55] Jüri Reimand, Meelis Kull, Hedi Peterson, Jaanus Hansen, and Jaak Vilo. G:Profiler–a web-based toolset for functional profiling of gene lists from large-scale experiments. *Nucleic Acids Res*, 35(Web Server issue):W193–200, July 2007.

[56] Uku Raudvere, Liis Kolberg, Ivan Kuzmin, Tambet Arak, Priit Adler, Hedi Peterson, and Jaak Vilo. G:Profiler: A web server for functional enrichment analysis and conversions of gene lists (2019 update). *Nucleic Acids Res*, 47(W1):W191–W198, July 2019.

[57] Zizhen Yao, Cindy T. J. van Velthoven, Michael Kunst, Meng Zhang, Delissa McMillen, Changkyu Lee, Won Jung, Jeff Goldy, Aliya Abdelhak, Matthew Aitken, Katherine Baker, Pamela Baker, Eliza Barkan, Darren Bertagnolli, Ashwin Bhandiwad, Cameron Bielstein, Prajal Bishwakarma, Jazmin Campos, Daniel Carey, Tamara Casper, Anish Bhaswanth Chakka, Rushil Chakrabarty, Sakshi Chavan, Min Chen, Michael Clark, Jennie Close, Kirsten Crichton, Scott Daniel, Peter DiValentin, Tim Dolbeare, Lauren Ellingwood, Elysha Fiabane, Timothy Fliss, James Gee, James Gerstenberger, Alexandra Glandon, Jessica Gloe, Joshua Gould, James Gray, Nathan Guilford, Junitta Guzman, Daniel Hirschstein, Windy Ho, Marcus Hooper, Mike

Huang, Madie Hupp, Kelly Jin, Matthew Kroll, Kanan Lathia, Arielle Leon, Su Li, Brian Long, Zach Madigan, Jessica Malloy, Jocelin Malone, Zoe Maltzer, Naomi Martin, Rachel McCue, Ryan McGinty, Nicholas Mei, Jose Melchor, Emma Meyerdierks, Tyler Mollenkopf, Skyler Moonsman, Thuc Nghi Nguyen, Sven Otto, Trangthanh Pham, Christine Rimorin, Augustin Ruiz, Raymond Sanchez, Lane Sawyer, Nadiya Shapovalova, Noah Shepard, Cliff Slaughterbeck, Josef Sulc, Michael Tieu, Amy Torkelson, Herman Tung, Nasmil Valera Cuevas, Shane Vance, Katherine Wadhwani, Katelyn Ward, Boaz Levi, Colin Farrell, Rob Young, Brian Staats, Ming-Qiang Michael Wang, Carol L. Thompson, Shoaib Mufti, Chelsea M. Pagan, Lauren Kruse, Nick Dee, Susan M. Sunkin, Luke Esposito, Michael J. Hawrylycz, Jack Waters, Lydia Ng, Kimberly Smith, Bosiljka Tasic, Xiaowei Zhuang, and Hongkui Zeng. A high-resolution transcriptomic and spatial atlas of cell types in the whole mouse brain. *Nature*, 624(7991):317–332, December 2023.

[58] Ao Chen, Yidi Sun, Ying Lei, Chao Li, Sha Liao, Juan Meng, Yiqin Bai, Zhen Liu, Zhifeng Liang, Zhiyong Zhu, Nini Yuan, Hao Yang, Zihan Wu, Feng Lin, Kexin Wang, Mei Li, Shuzhen Zhang, Meisong Yang, Tianyi Fei, Zhenkun Zhuang, Yiming Huang, Yong Zhang, Yuanfang Xu, Luman Cui, Ruiyi Zhang, Lei Han, Xing Sun, Bichao Chen, Wenjiao Li, Baoqian Huangfu, Kailong Ma, Jianyun Ma, Zhao Li, Yikun Lin, He Wang, Yanqing Zhong, Huifang Zhang, Qian Yu, Yaqian Wang, Xing Liu, Jian Peng, Chuanyu Liu, Wei Chen, Wentao Pan, Yingjie An, Shihui Xia, Yanbing Lu, Mingli Wang, Xinxiang Song, Shuai Liu, Zhifeng Wang, Chun Gong, Xin Huang, Yue Yuan, Yun Zhao, Qinwen Chai, Xing Tan, Jianfeng Liu, Mingyuan Zheng, Shengkang Li, Yaling Huang, Yan Hong, Zirui Huang, Min Li, Mengmeng Jin, Yan Li, Hui Zhang, Suhong Sun, Li Gao, Yinqi Bai, Mengnan Cheng, Guohai Hu, Shiping Liu, Bo Wang, Bin Xiang, Shuting Li, Huanhuan Li, Mengni Chen, Shiwen Wang, Minglong Li, Weibin Liu, Xin Liu, Qian Zhao, Michael Lisby, Jing Wang, Jiao Fang, Yun Lin, Qing Xie, Zhen Liu, Jie He, Huatai Xu, Wei Huang, Jan Mulder, Huanming Yang, Yangang Sun, Mathias Uhlen, Muming Poo, Jian Wang, Jianhua Yao, Wu Wei, Yuxiang Li, Zhiming Shen, Longqi Liu, Zhiyong Liu, Xun Xu, and Chengyu Li. Single-cell spatial transcriptome reveals cell-type organization in the macaque cortex. *Cell*, 186(17):3726–3743.e24, August 2023.

[59] Sierra Danielle Palumbos. *Molecular Determinants of Electrical Synaptic Specificity*. Thesis, November 2021.

[60] Abagael M Lasseigne, Fabio A Echeverry, Sundas Ijaz, Jennifer Carlisle Michel, E Anne Martin, Audrey J Marsh, Elisa Trujillo, Kurt C Marsden, Alberto E Pereda, and Adam C Miller. Electrical synaptic transmission requires a postsynaptic scaffolding protein. *eLife*, 10:e66898, April 2021.

[61] Irene Kahr, Karl Vandepoele, and Frans van Roy. Delta-protocadherins in health and disease. *Prog Mol Biol Transl Sci*, 116:169–192, 2013.

[62] Sarah E.W. Light and James D. Jontes. δ-Protocadherins: Organizers of neural circuit assembly. *Semin Cell Dev Biol*, 69:83–90, September 2017.

[63] Stacey Peek, Kar Men Mah, and Joshua A. Weiner. Regulation of Neural Circuit Formation by Protocadherins. *Cell Mol Life Sci*, 74(22):4133–4157, November 2017.

[64] Adam J Bisogni, Shila Ghazanfar, Eric O Williams, Heather M Marsh, Jean YH Yang, and David M Lin. Tuning of delta-protocadherin adhesion through combinatorial diversity. *eLife*, 7:e41050, December 2018.

[65] Ulrika Roine, Timo Roine, Juha Salmi, Taina Nieminen-von Wendt, Pekka Tani, Sami Leppämäki, Pertti Rintahaka, Karen Caeyenberghs, Alexander Leemans, and Mikko Sams. Abnormal wiring of the connectome in adults with high-functioning autism spectrum disorder. *Molecular Autism*, 6(1):65, December 2015.

[66] Seok-Jun Hong, Reinder Vos de Wael, Richard A. I. Bethlehem, Sara Lariviere, Casey Paquola, Sofie L. Valk, Michael P. Milham, Adriana Di Martino, Daniel S. Margulies, Jonathan Smallwood, and Boris C. Bernhardt. Atypical functional connectome hierarchy in autism. *Nat Commun*, 10(1):1022, March 2019.

[67] Dmitry Velmeshev, Lucas Schirmer, Diane Jung, Maximilian Haeussler, Yonatan Perez, Simone Mayer, Aparna Bhaduri, Nitasha Goyal, David H. Rowitch, and Arnold R. Kriegstein. Single-cell genomics identifies cell type–specific molecular changes in autism. *Science*, 364(6441):685–689, May 2019.

[68] Nasna Nassir, Asma Bankapur, Bisan Samara, Abdulrahman Ali, Awab Ahmed, Ibrahim M. Inuwa, Mehdi Zarrei, Seyed Ali Safizadeh Shabestari, Ammar AlBanna, Jennifer L. Howe, Bakhrom K. Berdiev, Stephen W. Scherer, Marc Woodbury-Smith, and Mohammed Uddin. Single-cell transcriptome identifies molecular subtype of autism spectrum disorder impacted by de novo loss-of-function variants regulating glial cells. *Human Genomics*, 15(1):68, November 2021.

[69] Chong Li, Jonas Simon Fleck, Catarina Martins-Costa, Thomas R. Burkard, Jan Themann, Marlene Stuempflen, Angela Maria Peer, Ábel Vertesy, Jamie B. Littleboy, Christopher Esk, Ulrich Elling, Gregor Kasprian, Nina S. Corsini, Barbara Treutlein, and Juergen A. Knoblich. Single-cell brain organoid screening identifies developmental defects in autism. *Nature*, 621(7978):373–380, September 2023.

[70] Felice A Dunn and Rachel O L Wong. Wiring patterns in the mouse retina: Collecting evidence across the connectome, physiology and light microscopy. *J Physiol*, 592(Pt 22):4809–4823, November 2014.

[71] Le Cong, F. Ann Ran, David Cox, Shuailiang Lin, Robert Barretto, Naomi Habib, Patrick D. Hsu, Xuebing Wu, Wenyan Jiang, Luciano A. Marraffini, and Feng Zhang. Multiplex genome engineering using CRISPR/Cas systems. *Science*, 339(6121):819–823, February 2013.

[72] Prashant Mali, Luhan Yang, Kevin M. Esvelt, John Aach, Marc Guell, James E. DiCarlo, Julie E. Norville, and George M. Church. RNA-guided human genome engineering via Cas9. *Science*, 339(6121):823–826, February 2013.

[73] Sumeet Sarin, Elizabeth Zuniga-Sanchez, Yerbol Z. Kurmangaliyev, Henry Cousins, Mili Patel, Jeanette Hernandez, Kelvin X. Zhang, Melanie A. Samuel, Marta Morey, Joshua R. Sanes, and S. Lawrence Zipursky. Role for Wnt Signaling in Retinal Neuropil Development: Analysis via RNA-Seq and In Vivo Somatic CRISPR Mutagenesis. *Neuron*, 98(1):109–126.e8, April 2018.

[74] Feng Tian, Yuyan Cheng, Songlin Zhou, Qianbin Wang, Aboozar Monavarfeshani, Kun Gao, Weiqian Jiang, Riki Kawaguchi, Qing Wang, Mingjun Tang, Ryan Donahue, Huyan Meng, Yu Zhang, Anne Jacobi, Wenjun Yan, Jiani Yin, Xinyi Cai, Zhiyun Yang, Shane Hegarty, Joanna Stanicka, Phillip Dmitriev, Daniel Taub, Junjie Zhu, Clifford J. Woolf, Joshua R. Sanes, Daniel H. Geschwind, and Zhigang He. Core transcription programs controlling injury-induced neurodegeneration of retinal ganglion cells. *Neuron*, 110(16):2607–2624.e8, August 2022.

[75] Sayantanee Biswas, Michelle R. Emond, Kurtis P. Chenoweth, and James D. Jontes. δ-Protocadherins regulate neural progenitor cell division by antagonizing Ryk and Wnt/β-catenin signaling. *iScience*, 24(8):102932, July 2021.

[76] Yifeng Zhang, In-Jung Kim, Joshua R. Sanes, and Markus Meister. The most numerous ganglion cell type of the mouse retina is a selective feature detector. *Proc Natl Acad Sci U S A*, 109(36):E2391–E2398, September 2012.

[77] Brenna Krieger, Mu Qiao, David L. Rousso, Joshua R. Sanes, and Markus Meister. Four alpha ganglion cell types in mouse retina: Function, structure, and molecular signatures. *PLOS ONE*, 12(7):e0180091, July 2017.

[78] Daniel J. Dickinson and Bob Goldstein. CRISPR-Based Methods for Caenorhabditis elegans Genome Engineering. *Genetics*, 202(3):885–901, March 2016.

[79] Scott J. Gratz, C. Dustin Rubinstein, Melissa M. Harrison, Jill Wildonger, and Kate M. O'Connor-Giles. CRISPR-Cas9 genome editing in Drosophila. *Curr Protoc Mol Biol*, 111:31.2.1–31.2.20, July 2015.

[80] Mingyu Li, Liyuan Zhao, Patrick Page-McCaw, and Wenbiao Chen. Zebrafish genome engineering using the CRISPR-Cas9 system. *Trends Genet*, 32(12):815–827, December 2016.

[81] Kristofer Davie, Jasper Janssens, Duygu Koldere, Maxime De Waegeneer, Uli Pech, Łukasz Kreft, Sara Aibar, Samira Makhzami, Valerie Christiaens, Carmen Bravo González-Blas, Suresh Poovathingal, Gert Hulselmans, Katina I. Spanier, Thomas Moerman, Bram Vanspauwen, Sarah Geurs, Thierry Voet, Jeroen Lammertyn, Bernard Thienpont, Sha Liu, Nikos Konstantinides, Mark Fiers, Patrik Verstreken, and Stein Aerts. A Single-Cell Transcriptome Atlas of the Aging Drosophila Brain. *Cell*, 174(4):982–998.e20, August 2018.

[82] Sven Dorkenwald, Arie Matsliah, Amy R Sterling, Philipp Schlegel, Szi-chieh Yu, Claire E. McKellar, Albert Lin, Marta Costa, Katharina Eichler, Yijie Yin, Will Silversmith, Casey Schneider-Mizell, Chris S. Jordan, Derrick Brittain, Akhilesh Halageri, Kai Kuehner, Oluwaseun Ogedengbe, Ryan Morey, Jay Gager, Krzysztof Kruk, Eric Perlman, Runzhe Yang, David Deutsch, Doug Bland, Marissa Sorek, Ran Lu, Thomas Macrina, Kisuk Lee, J. Alexander Bae, Shang Mu, Barak Nehoran, Eric Mitchell, Sergiy Popovych, Jingpeng Wu, Zhen Jia, Manuel Castro, Nico Kemnitz, Dodam Ih, Alexander Shakeel Bates, Nils Eckstein, Jan Funke, Forrest Collman, Davi D. Bock, Gregory S.X.E Jefferis, H. Sebastian Seung, and Mala Murthy. Neuronal wiring diagram of an adult brain. *bioRxiv*, page 2023.06.27.546656, July 2023.

[83] Bosiljka Tasic, Vilas Menon, Thuc Nghi Nguyen, Tae Kyung Kim, Tim Jarsky, Zizhen Yao, Boaz Levi, Lucas T. Gray, Staci A. Sorensen, Tim Dolbeare, Darren Bertagnolli, Jeff Goldy, Nadiya Shapovalova, Sheana Parry, Changkyu Lee, Kimberly Smith, Amy Bernard, Linda Madisen, Susan M. Sunkin, Michael Hawrylycz, Christof Koch, and Hongkui Zeng. Adult mouse cortical cell taxonomy revealed by single cell transcriptomics. *Nat. Neurosci.*, 19(2):335–346, February 2016.

[84] Bosiljka Tasic, Zizhen Yao, Lucas T. Graybuck, Kimberly A. Smith, Thuc Nghi Nguyen, Darren Bertagnolli, Jeff Goldy, Emma Garren, Michael N. Economo, Sarada Viswanathan, Osnat Penn, Trygve Bakken, Vilas Menon, Jeremy Miller, Olivia Fong, Karla E. Hirokawa, Kanan Lathia, Christine Rimorin, Michael Tieu, Rachael Larsen, Tamara Casper, Eliza Barkan, Matthew Kroll, Sheana Parry, Nadiya V. Shapovalova, Daniel Hirschstein, Julie Pendergraft, Heather A. Sullivan, Tae Kyung Kim, Aaron Szafer, Nick Dee, Peter Groblewski, Ian Wickersham, Ali Cetin, Julie A. Harris, Boaz P. Levi, Susan M. Sunkin, Linda Madisen, Tanya L. Daigle, Loren Looger, Amy Bernard, John Phillips, Ed Lein, Michael Hawrylycz, Karel Svoboda, Allan R. Jones, Christof Koch, and Hongkui Zeng. Shared and distinct transcriptomic cell types across neocortical areas. *Nature*, 563(7729):72–78, November 2018.

[85] Zizhen Yao, Cindy T. J. van Velthoven, Thuc Nghi Nguyen, Jeff Goldy, Adriana E. Sedeno-Cortes, Fahimeh Baftizadeh, Darren Bertagnolli, Tamara Casper, Megan Chiang, Kirsten Crichton, Song-Lin Ding, Olivia Fong, Emma Garren, Alexandra Glandon, Nathan W. Gouwens, James Gray, Lucas T. Graybuck, Michael J. Hawrylycz, Daniel Hirschstein, Matthew Kroll, Kanan Lathia, Changkyu Lee, Boaz Levi, Delissa McMillen, Stephanie Mok, Thanh Pham, Qingzhong Ren, Christine Rimorin, Nadiya Shapovalova, Josef Sulc, Susan M. Sunkin, Michael Tieu, Amy Torkelson, Herman Tung, Katelyn Ward, Nick Dee, Kimberly A. Smith, Bosiljka Tasic, and Hongkui Zeng. A taxonomy of transcriptomic cell types across the isocortex and hippocampal formation. *Cell*, 184(12):3222–3241.e26, June 2021.

[86] Davi D. Bock, Wei-Chung Allen Lee, Aaron M. Kerlin, Mark L. Andermann, Greg Hood, Arthur W. Wetzel, Sergey Yurgenson, Edward R. Soucy, Hyon Suk Kim, and R. Clay Reid. Network anatomy and in vivo physiology of visual cortical neurons. *Nature*, 471(7337):177–182, March 2011.

[87] Wei-Chung Allen Lee, Vincent Bonin, Michael Reed, Brett J. Graham, Greg Hood, Katie Glattfelder, and R. Clay Reid. Anatomy and function of an excitatory network in the visual cortex. *Nature*, 532(7599):370–374, April 2016.

[88] Shenqin Yao, Quanxin Wang, Karla E. Hirokawa, Benjamin Ouellette, Ruweida Ahmed, Jasmin Bomben, Krissy Brouner, Linzy Casal, Shiella Caldejon, Andy Cho, Nadezhda I. Dotson, Tanya L. Daigle, Tom Egdorf, Rachel Enstrom, Amanda Gary, Emily Gelfand, Melissa Gorham, Fiona Griffin, Hong Gu, Nicole Hancock, Robert Howard, Leonard Kuan, Sophie Lambert, Eric Kenji Lee, Jennifer Luviano, Kyla Mace, Michelle Maxwell, Marty T. Mortrud, Maitham Naeemi, Chelsea Nayan, Nhan-Kiet Ngo, Thuyanh Nguyen, Kat North, Shea Ransford, Augustin Ruiz, Sam Seid, Jackie Swapp, Michael J. Taormina, Wayne Wakeman, Thomas Zhou, Philip R.

Nicovich, Ali Williford, Lydia Potekhina, Medea McGraw, Lydia Ng, Peter A. Groblewski, Bosiljka Tasic, Stefan Mihalas, Julie A. Harris, Ali Cetin, and Hongkui Zeng. A whole-brain monosynaptic input connectome to neuron classes in mouse visual cortex. *Nat Neurosci*, 26(2):350–364, February 2023.

[89] Xiaoyin Chen, Yu-Chi Sun, Huiqing Zhan, Justus M. Kebschull, Stephan Fischer, Katherine Matho, Z. Josh Huang, Jesse Gillis, and Anthony M. Zador. High-Throughput Mapping of Long-Range Neuronal Projection Using In Situ Sequencing. *Cell*, 179(3):772–786.e19, October 2019.

[90] Yu-Chi Sun, Xiaoyin Chen, Stephan Fischer, Shaina Lu, Huiqing Zhan, Jesse Gillis, and Anthony M. Zador. Integrating barcoded neuroanatomy with spatial transcriptional profiling enables identification of gene correlates of projections. *Nat Neurosci*, 24(6):873–885, June 2021.

[91] Nicole Y. Tsai, Fei Wang, Kenichi Toma, Chen Yin, Jun Takatoh, Emily L. Pai, Kongyan Wu, Angela C. Matcham, Luping Yin, Eric J. Dang, Denise K. Marciano, John L. Rubenstein, Fan Wang, Erik M. Ullian, and Xin Duan. Trans-Seq maps a selective mammalian retinotectal synapse instructed by Nephronectin. *Nat Neurosci*, 25(5):659–674, May 2022.

[92] Aixin Zhang, Lei Jin, Shenqin Yao, Makoto Matsuyama, Cindy van Velthoven, Heather Sullivan, Na Sun, Manolis Kellis, Bosiljka Tasic, Ian R. Wickersham, and Xiaoyin Chen. Rabies virus-based barcoded neuroanatomy resolved by single-cell RNA and in situ sequencing. *bioRxiv*, page 2023.03.16.532873, November 2023.

[93] Krystyna Mazan-Mamczarz, Jisu Ha, Supriyo De, and Payel Sen. Single-Cell Analysis of the Transcriptome and Epigenome. *Methods Mol Biol*, 2399:21–60, 2022.

[94] Hayley M. Bennett, William Stephenson, Christopher M. Rose, and Spyros Darmanis. Single-cell proteomics enabled by next-generation sequencing or mass spectrometry. *Nat Methods*, 20(3):363–374, March 2023.

[95] Tian Wang, Yuri M. Brovman, and Sriganesh Madhvanath. Personalized Embedding-based e-Commerce Recommendations at eBay. *arXiv preprint arXiv:2102.06156*, February 2021.

[96] Yantao Yu, Weipeng Wang, Zhoutian Feng, and Daiyue Xue. A dual augmented two-tower model for online large-scale recommendation. *KDD*, 2021.